

Latent Causal Diffusions for Single-Cell Perturbation Modeling

Lars Lorch^a, Jiaqi Zhang^{b,c}, Charlotte Bunne^{d,e},
 Andreas Krause^{a,*}, Bernhard Schölkopf^{f,g,a,*}, and Caroline Uhler^{b,c,*}

^aDepartment of Computer Science, ETH Zürich, Zürich, Switzerland

^bLaboratory for Information and Decision Systems, Massachusetts Institute of Technology, Cambridge, MA, USA

^cEric and Wendy Schmidt Center, Broad Institute of MIT and Harvard, Cambridge, MA, USA

^dSchool of Computer and Communication Sciences, EPFL, Lausanne, Switzerland

^eSwiss Institute for Experimental Cancer Research, School of Life Sciences, EPFL, Lausanne, Switzerland

^fMax Planck Institute for Intelligent Systems, Tübingen, Germany

^gELLIS Institute, Tübingen, Germany

*Correspondence to: krausea@ethz.ch, bs@tuebingen.mpg.de, cuhler@mit.edu

Abstract

Perturbation screens hold the potential to systematically map regulatory processes at single-cell resolution, yet modeling and predicting transcriptome-wide responses to perturbations remains a major computational challenge. Existing methods often underperform simple baselines, fail to disentangle measurement noise from biological signal, and provide limited insight into the causal structure governing cellular responses. Here, we present the latent causal diffusion (LCD), a generative model that frames single-cell gene expression as a stationary diffusion process observed under measurement noise. LCD outperforms established approaches in predicting the distributional shifts of unseen perturbation combinations in single-cell RNA-sequencing screens while simultaneously learning a mechanistic dynamical system of gene regulation. To interpret these learned dynamics, we develop an approach we call causal linearization via perturbation responses (CLIPR), which yields an approximation of the direct causal effects between all genes modeled by the diffusion. CLIPR provably identifies causal effects under a linear drift assumption and recovers causal structure in both simulated systems and a genome-wide perturbation screen, where it clusters genes into coherent functional modules and resolves causal relationships that standard differential expression analysis cannot. The LCD-CLIPR framework bridges generative modeling with causal inference to predict unseen perturbation effects and map the underlying regulatory mechanisms of the transcriptome.

Introduction

Genome-wide perturbation screens now enable causal interrogation of gene function at single-cell resolution (1, 2). As these screens scale to capture the transcriptomic effects of thousands of individual gene perturbations, the central challenge shifts from data collection to modeling regulatory interactions and predicting the outcomes of multi-gene combinations. Genetic interactions are often nonlinear, with the effects of combined perturbations deviating from the sum of their individual effects (3, 4). Because the combinatorial search space grows exponentially, exhaustive experimental assays quickly become infeasible (5, 6). Mapping the genetic circuitry of cellular programs thus requires computational causal models that can generalize from observed data to predict the effects of unseen perturbation combinations and reveal the mechanisms governing their interactions (3, 7–10).

While deep learning has advanced representation learning for single-cell biology, current models often struggle to outperform simple, domain-aware baselines when predicting post-perturbation responses (11–13). Foundation models pre-trained on large single-cell atlases, for instance, frequently fail to predict gene expression changes for held-out perturbations more accurately than additive heuristics (14–16). Neural network models trained on individual perturbation screens typically focus on average effects, neglecting the heterogeneity and stochasticity that define cellular states (15, 17). Furthermore, these

models rarely account for measurement noise, often conflating technical artifacts with biological signal (18–20). Above all, these architectures remain largely opaque, failing to characterize how perturbations propagate through genetic pathways to drive transcriptional changes. Consequently, current methods provide limited structural insight into the causal mechanisms that govern cellular responses.

In this work, we introduce single-cell perturbation modeling based on the latent causal diffusion (LCD), a generative model that frames gene expression as a latent stationary dynamical system observed under measurement noise (21, 22). We formalize gene regulation as a diffusion process governed by a system of stochastic differential equations (SDEs), where each gene’s expression evolves mechanistically as a function of its regulators. By assuming this diffusion process operates in equilibrium (23–26), we can infer the functional causal mechanisms of the SDEs without direct observation of the temporal dynamics, viewing single-cell data as samples from the stationary distribution under a measurement model (27–29). Unlike previous deep learning approaches, this enables identifying causal data-generating mechanisms while explicitly decoupling biological stochasticity from technical noise. We model perturbations of the transcriptome as modifications to the underlying gene regulatory mechanisms, causing the diffusion to reach a different equilibrium. When applied to large-scale Perturb-seq screens (4, 5), LCDs predicted the distributional shifts of unseen perturbation combinations more accurately than established approaches while learning an explicit, gene-level dynamical system as the generative model.

The regulatory dynamics learned by LCDs are parameterized by neural networks, so we render their causal dependencies interpretable by developing CLIPR, a linearization technique that approximates the direct gene-gene causal effects modeled in the diffusion process. For linear systems, CLIPR provably identifies causal effects by leveraging how drift perturbations behave at a control state and in equilibrium. In nonlinear systems, it provides the minimum-norm linear causal effects that best approximate the drift’s response to perturbations. We validated CLIPR on simulated systems, demonstrating that it reliably recovers ground-truth causal structures from complex neural network drifts. Finally, by applying LCD and CLIPR to a genome-wide Perturb-seq assay (1), we uncovered regulatory mechanisms in K562 cells that remain hidden under standard differential expression analysis, providing a scalable framework for mapping causal dependencies in the cell.

Results

A causal generative model of the transcriptome

Latent causal diffusions model the joint expression of d genes in a cell as a stochastic process $\mathbf{x}(t) \in \mathbb{R}^d$ evolving over time t , as gene expression is inherently stochastic (24, 30, 31). Each gene g is represented by a random state $x_g(t)$, corresponding to a noiseless, unobserved version of expression, that evolves according to a stochastic differential equation (SDE) (32)

$$dx_g(t) = [f(\mathbf{x}(t))]_g dt + \sigma d\mathbb{W}_g(t), \quad (1)$$

where $\mathbb{W}_g(t)$ denotes standard Brownian motion. The drift function $f : \mathbb{R}^d \rightarrow \mathbb{R}^d$ models the causal regulatory mechanisms among the genes, and the diffusion term captures stochastic fluctuations with scale σ . The joint stochastic process $\mathbf{x}(t)$, obtained by solving the coupled SDEs for all genes, defines the distribution over cell states at time t (Fig. 1A, bottom).

LCDs model the process $\mathbf{x}(t)$ as *stationary*, so the SDEs induce a time-independent distribution $p(\mathbf{x})$ over gene states. Steady-state models are canonically used as mathematical descriptions of gene expression (23–26). The stationarity assumption enables inference of the causal dynamics f directly from the state distribution $p(\mathbf{x})$, without requiring time-resolved observations of $\mathbf{x}(t)$ itself (Fig. 1A, center) (21, 29). The time dimension of LCDs allows modeling gene feedback loops by implicitly unrolling causal effects over time, akin to biological systems (33–35). This concept of time differs from recent diffusion-based models, which either model time series (36, 37) or treat time as computation steps rather than a physical timescale of gene regulation (38).

We parameterize the drift f by a neural network that shares parameters across the causal mechanisms of each gene (Fig. 1B). Specifically, $[f(\mathbf{x})]_g$ and $[f(\mathbf{x})]_{g'}$ share a hidden state, reflecting the substantial structure of gene regulatory circuits (39–42). In our experiments, the shared hidden dynamics enabled

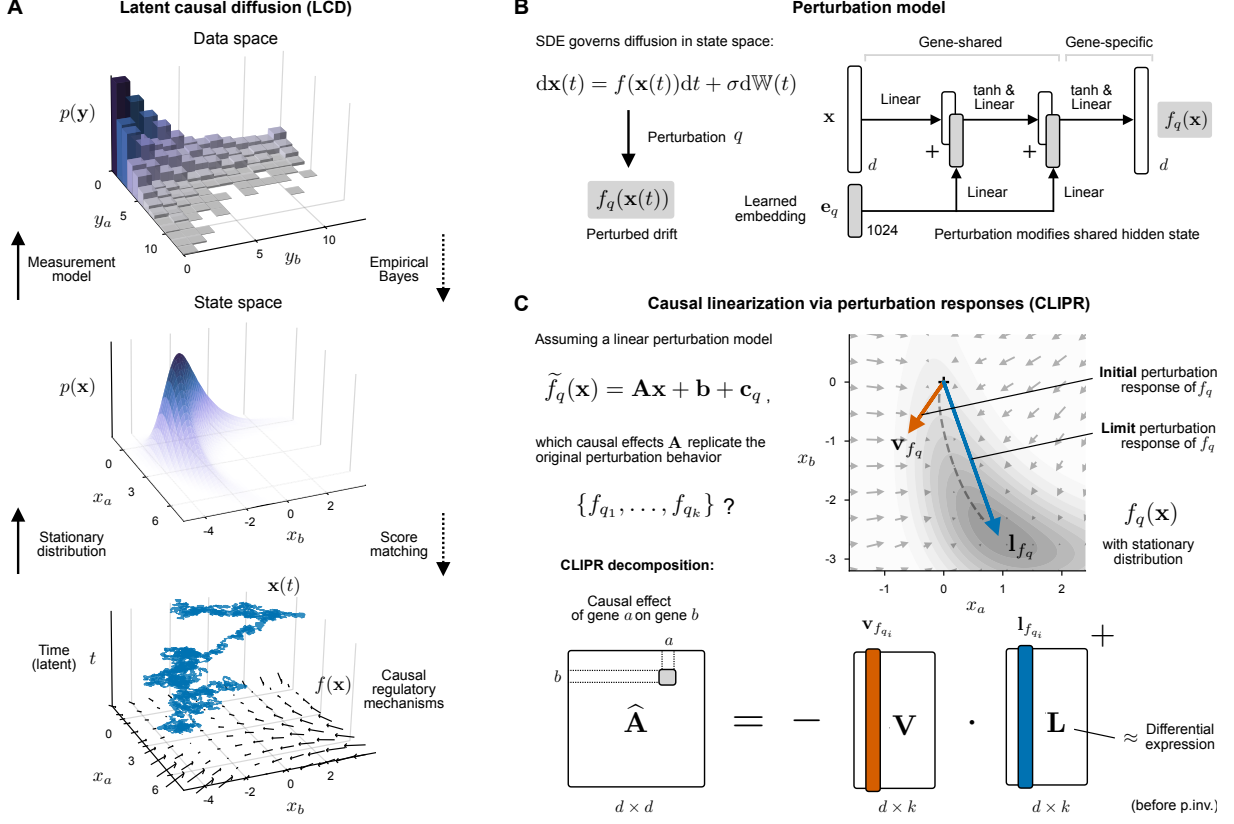


Figure 1: The latent causal diffusion (LCD) model and CLIPR. (A) LCDs model single-cell expression data \mathbf{y} (top) as noisy observations of unobserved, noiseless gene states \mathbf{x} (center). States \mathbf{x} are samples from a stationary stochastic process $\mathbf{x}(t)$ evolving under the causal regulatory dynamics $f(\mathbf{x})$ of an SDE (bottom). To train LCDs, we first infer $p(\mathbf{x})$ via empirical Bayes, then learn f in state space via score matching. (B) Dynamics f explicitly model gene regulation and are parameterized by a neural network with shared hidden state across genes. Perturbations modify this hidden state via learned embeddings \mathbf{e}_q . (C) To interpret the causal dependencies in f , we estimate a linear causal matrix that induces the perturbation behavior of f (left). This matrix is computed from the initial (\mathbf{v}_{f_q}) and limit (\mathbf{l}_{f_q}) responses when f is perturbed. The limit response is approximated by following the vector field flow until convergence (right).

LCDs to scale to modeling a thousand genes jointly. We model perturbations as shifts in this hidden state, computed from learned embedding vectors \mathbf{e}_q , where q is the index of a perturbation (Fig. 1B), as gene expressions tend to co-vary across perturbations, and perturbations cluster by their shared transcriptomic effects (39, 40, 43). Combinations of perturbations are represented as additive compositions of these embeddings. Perturbations thus act on the regulatory mechanisms of f rather than directly on gene expression, forcing the diffusion to converge to a new steady state. We write f_q to denote the dynamics f under perturbation q .

We do not observe the state distribution $p(\mathbf{x})$ directly but instead through noisy measurements of single cells. LCDs model each single-cell count vector $\mathbf{y} \in \mathbb{N}^d$ as an independent sample from the latent stationary diffusion, observed under a zero-inflated Poisson (ZIP) likelihood (28, 29)

$$p(y_g | x_g; \pi_g) = \text{ZIP}(y_g; \mu_g(x_g), \pi_g) \quad (2)$$

with dropout probability π_g . Here, $\mu_g : \mathbb{R} \rightarrow \mathbb{R}^+$ is a link function with fixed, gene-specific scaling that maps states x_g to nonnegative Poisson rates. If the Poisson rate follows a Gamma distribution, the distribution of y_g has a zero-inflated negative binomial form, which corresponds to the steady-state of the promoter-activation model commonly characterizing scRNA-seq data (26, 27, 44). LCDs generalize this to richer distributions $p(\mathbf{y})$ by capturing causal dependencies among genes in $p(\mathbf{x})$ (Fig. 1A, top).

To infer the model from data, we view a perturbation screen as a collection of count distributions, one per perturbation q_i , where q_0 represents the unperturbed setting ($f_{q_0} = f$). Each count distribution arises from the same drift and measurement model, differing only by the perturbation-specific shifts in

the hidden state of f_{q_i} (29). To separate measurement and biological noise, we first infer the likelihood parameters π and state distribution $p(\mathbf{x})$ for each perturbation condition. We then jointly fit the dynamics f and perturbation embeddings \mathbf{e}_q to all inferred state distributions (Methods).

Estimating causal dependencies in stationary diffusions

A learned LCD models a causal generative process, in which genes mechanistically regulate one another, but the dynamics of LCDs are not directly interpretable, since the drift $f(\mathbf{x}(t))$ is nonlinear and depends on $\mathbf{x}(t)$. However, perturbations of the drift $\{f_{q_1}, \dots, f_{q_k}\}$ reveal key regulatory mechanisms modeled by f . We can leverage this perturbation behavior to obtain a linearization of the system that preserves its overall perturbation responses, enabling us to interpret the causal structure of a learned LCD drift f .

The key idea is to ask: what *linear* drift \tilde{f} would replicate the perturbation behavior of $\{f_{q_1}, \dots, f_{q_k}\}$ (Fig. 1C, left)? We show that such a linear approximation can be estimated in closed form from simple properties of the perturbed drifts f_{q_i} . Since linear systems describe gene-gene regulation by a single parameter per pair, they yield an interpretable approximation of the regulatory dynamics of f . We consider linear SDEs (Eq. 1) with drift

$$\tilde{f}_q(\mathbf{x}) = \mathbf{A}\mathbf{x} + \mathbf{b} + \mathbf{c}_q, \quad (3)$$

where $\mathbf{A} \in \mathbb{R}^{d \times d}$ and $\mathbf{b} \in \mathbb{R}^d$ are causal effect and bias parameters, $\mathbf{c}_q \in \mathbb{R}^d$ models a perturbation q , and the real part of the maximum eigenvalue $\Re(\lambda_{\max}(\mathbf{A}))$ is strictly negative. Linear SDEs of this form have a unique Gaussian stationary distribution with mean (45)

$$\boldsymbol{\mu}_q = -\mathbf{A}^{-1}(\mathbf{b} + \mathbf{c}_q). \quad (4)$$

We can describe the perturbation f_q of a drift f by two intuitive properties: the drift vector acting at a control state and the steady state it induces. To formalize these properties, we use the zero vector $\mathbf{0}$ as the control state, which represents the mean of a standardized, unperturbed linear system. We then define the *initial perturbation response* of f_q as

$$\mathbf{v}_{f_q} := f_q(\mathbf{0}), \quad (5)$$

and the *limit perturbation response* of f_q as the fixed point

$$\mathbf{l}_{f_q} := \mathbf{x}^* \quad \text{s.t.} \quad f_q(\mathbf{x}^*) = \mathbf{0}. \quad (6)$$

For the linear model, the post-perturbation mean $\boldsymbol{\mu}_q$ is the fixed point \mathbf{l}_{f_q} . Therefore, the limit perturbation response \mathbf{l}_{f_q} directly corresponds to differential expression, assuming the unperturbed system has mean $\mathbf{0}$. By contrast, the initial perturbation response \mathbf{v}_{f_q} represents the initial drift towards the post-perturbation steady state (Fig. 1C, right). We assume that a fixed point exists and can be approximated by integrating the drift flow (Methods).

Applying different perturbations q_i to a diffusion drift f yields different perturbation responses $\mathbf{v}_{f_{q_i}}$ and $\mathbf{l}_{f_{q_i}}$. Each respective perturbation outcome reveals key drivers of the dynamics f , and collectively they map how the system behaves under perturbations. Our theorem below shows that, given several perturbation response vectors, we can construct a linear causal effect matrix $\hat{\mathbf{A}}$ that replicates the same response vectors as the original perturbed drifts. Moreover, assuming the true drift is linear, sufficiently diverse perturbations identify all causal effects:

Theorem 1. *Let $\mathbf{v}_{f_{q_i}}$ and $\mathbf{l}_{f_{q_i}}$ be perturbation responses of a general drift f_q for perturbations $q_i \in \{q_1, \dots, q_k\}$. The linear drift matrix (Eq. 3) that approximates these perturbation response vectors with least-squares error and minimum Frobenius norm is given by*

$$\hat{\mathbf{A}} = -\mathbf{V}\mathbf{L}^+, \quad (7)$$

where $(\cdot)^+$ denotes the Moore-Penrose pseudoinverse, and $\mathbf{V}, \mathbf{L} \in \mathbb{R}^{d \times k}$ are matrices with i -th columns $\mathbf{v}_{f_{q_i}}$ and $\mathbf{l}_{f_{q_i}}$, respectively. Moreover, if the drift function is linear ($f_q = \tilde{f}_q$) and \mathbf{L} has full row rank, then $\hat{\mathbf{A}} = \mathbf{A}$.

Our proof is given in [SI Appendix](#). When the bias \mathbf{b} is generic, a sufficient condition for \mathbf{L} being full rank is that $k \geq d$ perturbation shift vectors \mathbf{c}_q are linearly independent. We refer to this system as the causal linearization via perturbation responses (CLIPR). In practice, we use a Tikhonov-regularized variant, which improves stability under model mismatch by trading off perturbation response fit against smaller norms of the causal effects \mathbf{A} via a scalar λ (see proof of Theorem 1):

$$\hat{\mathbf{A}}_\lambda = -\mathbf{V}\mathbf{L}^\top(\mathbf{L}\mathbf{L}^\top + \lambda\mathbf{I})^{-1}. \quad (8)$$

Theorem 1 has several implications. First, the identification result suggests that all single-gene perturbations can fully disentangle the causal effects in a linear system. Specifically, Theorem 1 shows that linear causal effects can be directly decomposed into (and uniquely identified by) the DEs \mathbf{L} and the drift forces \mathbf{V} at the control state $\mathbf{0}$ (Fig. 1C, right). While access to exact perturbation responses constitutes an idealized setting, the result provides a theoretical foundation for estimating \mathbf{A} by computing \mathbf{v}_{f_q} and \mathbf{l}_{f_q} for drifts f_q learned from finite samples and noisy observations.

Second, the simple form $\hat{\mathbf{A}} = -\mathbf{V}\mathbf{L}^+$ highlights a fundamental distinction between direct causal effects and differential expression. Under the simplifying assumptions discussed above, differential expression (DE), the mean change in expression induced by a perturbation, corresponds to the limit perturbation responses \mathbf{L} . CLIPR shows that DE, as captured by \mathbf{L} , is distinct from the direct causal effects among the genes themselves: DE emerges from unrolling direct causal effects \mathbf{A} over time. We say that gene a is a direct cause of gene b if b depends on perturbations of a when all other genes are held fixed (46). By definition of the drift (Eq. 3), \mathbf{A} encodes precisely these direct causal dependencies.

Third, CLIPR enables interpreting nonlinear drifts f_q , since \mathbf{v}_{f_q} and \mathbf{l}_{f_q} can be computed for any drift function that models perturbations. CLIPR then reveals the linear causal effects $\hat{\mathbf{A}}$ that best approximate the perturbation behavior of the original dynamics f_q . The regularized estimator $\hat{\mathbf{A}}_\lambda$ mitigates artifacts resulting from model mismatch when the linear model is overdetermined by the nonlinear responses, since it encourages smaller norms of \mathbf{A} in favor of overfitting the responses.

Fourth, the perturbation shifts \mathbf{c}_q in the approximated linear drift (Eq. 3) are *not* needed to compute the estimate $\hat{\mathbf{A}}$. What matters is that the original drift $f_q(\mathbf{x})$ can be evaluated and integrated to obtain \mathbf{V} and \mathbf{L} . This also implies that perturbations in the approximated linear drift (Eq. 3) neither need to have known targets nor affect single genes and could therefore also be, for example, induced by drugs. In fact, the following corollary shows that the perturbation shifts \mathbf{c}_q in the approximated linear model are implied by the CLIPR matrix $\hat{\mathbf{A}}$:

Corollary 2. *The bias $\hat{\mathbf{b}}$ and shift vectors $\hat{\mathbf{c}}_q$ of the linear model (Eq. 3) implied by the matrix $\hat{\mathbf{A}}$ of Theorem 1 are*

$$\hat{\mathbf{b}} = -\hat{\mathbf{A}}\mathbf{l}_f \quad \text{and} \quad \hat{\mathbf{c}}_q = \hat{\mathbf{A}}\mathbf{l}_{f_q} - \hat{\mathbf{A}}\mathbf{l}_f.$$

Perturbation effect prediction at single-cell resolution

We evaluated LCDs against established methods for predicting the effects of unseen perturbation combinations in Perturb-seq assays. Our evaluation used two datasets that contain both single-gene and double-gene perturbations, spanning different cell lines and CRISPR-Cas technologies (Norman et al. (4) and Wessels et al. (5); [SI Appendix, Table S1](#)). For both datasets, each method was trained on control samples, all single-gene perturbations, and a subset of double-gene perturbations. After training, methods predicted full single-cell distributions of the transcriptome for the held-out two-gene combinations. Using ten disjoint testing folds, we obtained held-out predictions for all two-gene perturbations in both screens ([SI Appendix, Fig. S1](#)).

We compared LCDs to various methods. Recent findings suggested that established approaches perform on par with additive heuristics (11, 12, 47). We thus evaluated an additive baseline called SALT and its variant PEPER, which learns a nonlinear correction on top of SALT (13). We also evaluated the deep-learning approaches CPA (19), which uses autoencoders, and GEARS (17), which learns graph neural networks over gene relationship graphs sourced from prior knowledge ([Methods](#)). We quantified prediction accuracy relative to the observed post-perturbation data using several metrics. Our primary

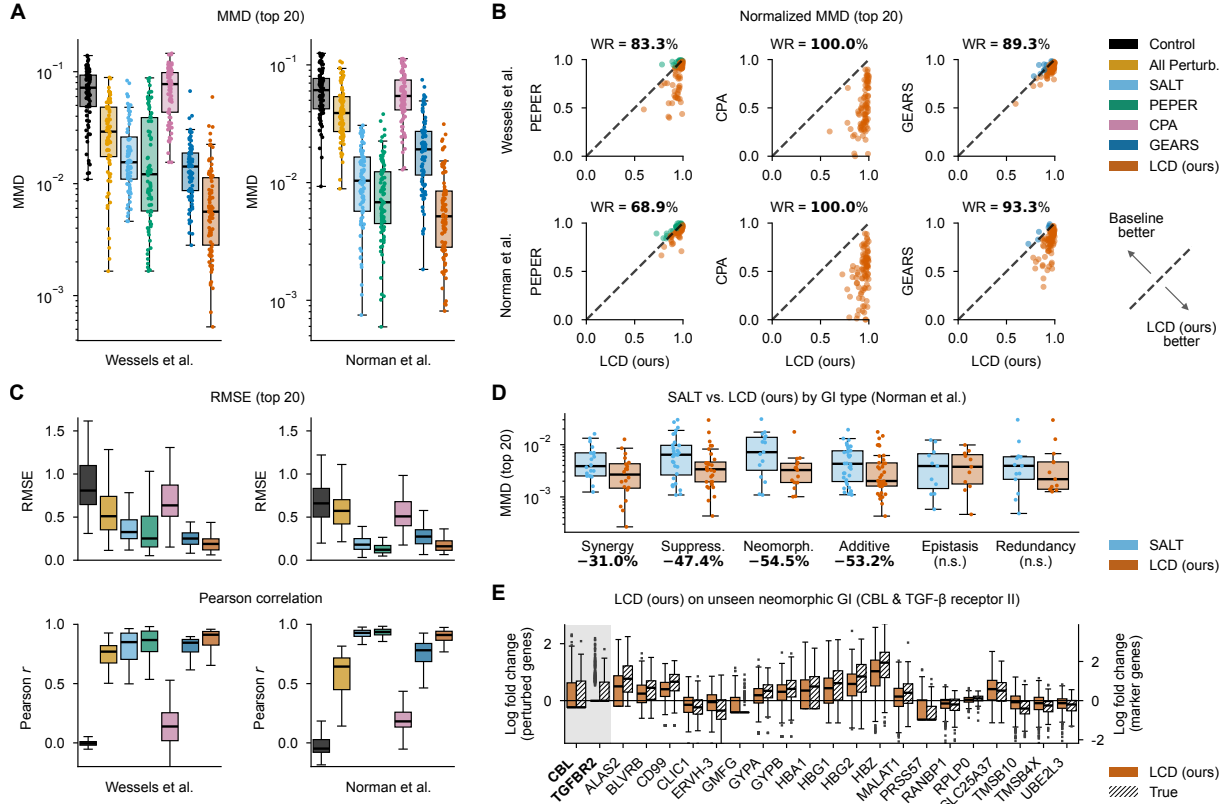


Figure 2: LCDs outperform state-of-the-art models at predicting combinatorial perturbation effects. (A) Maximum mean discrepancy (MMD) between predicted and observed single-cell expressions for held-out double-gene perturbations of the two datasets, computed on top 20 differentially expressed (DE) genes. Each dot represents one perturbation. Two leftmost bars show baseline performance of randomly sampled control and perturbed cells from all conditions. (B) Perturbation comparison of LCD with deep-learning baselines on MMD, normalized to [0, 1] across methods. Win rate (WR): proportion of perturbations where LCD achieved lower error. (C) Root mean squared error (RMSE) of predicted mean expression of top 20 DE genes (top) and Pearson correlation on full mean expression vector (bottom) (D) MMD stratified by genetic interaction (GI) type, comparing LCD and the additive baseline SALT. Axis labels indicate significant improvement per GI category (percentage reduction in median MMD by LCD) or not (n.s.; one-sided Wilcoxon signed-rank test, $P < 0.05$). (E) Predicted vs. observed expression for top 20 DE genes of a held-out perturbation with neomorphic GI. Grey section shows the perturbed genes (bold labels). All box plots show the median, interquartile range (IQR), and whiskers extend to farthest points within $1.5 \times$ IQR.

metric was the maximum mean discrepancy (MMD), which measures full distributional fit (18, 48). Low MMD implies the prediction matches all moments of the observed single-cell distribution, characterizing not only its means, but also its (co)variances, skewness, and tail-heaviness. Following prior work, we also report the root mean squared error (RMSE) and Pearson correlation of the means (17, 19). We mostly focused on metrics computed on the top 20 differentially expressed genes, as most genes often show negligible change under perturbation (17, 18).

LCDs significantly outperformed both the heuristics and established approaches in terms of overall distributional accuracy of the predicted single-cell transcriptomes (Fig. 2A). Per-perturbation comparisons on each dataset show that LCDs made more accurate predictions as measured by MMD than all other methods in more than roughly 80% of test perturbations (Fig. 2B). Only PEPER achieved comparable performance to LCDs on the screen by Norman et al., where more single-gene perturbations are available for calibrating its additive heuristic (98 for Norman et al. versus 5 for Wessels et al.; [SI Appendix, Table S1](#)), suggesting that LCDs disentangle individual gene contributions effectively from combined perturbations. When reducing the single-cell transcriptome to a mean expression vector, LCDs still provided the most accurate predictions across all baselines, though SALT and PEPER performed more competitively (Fig. 2C). LCDs thus achieved significant accuracy gains by modeling a full single-cell count distribution.

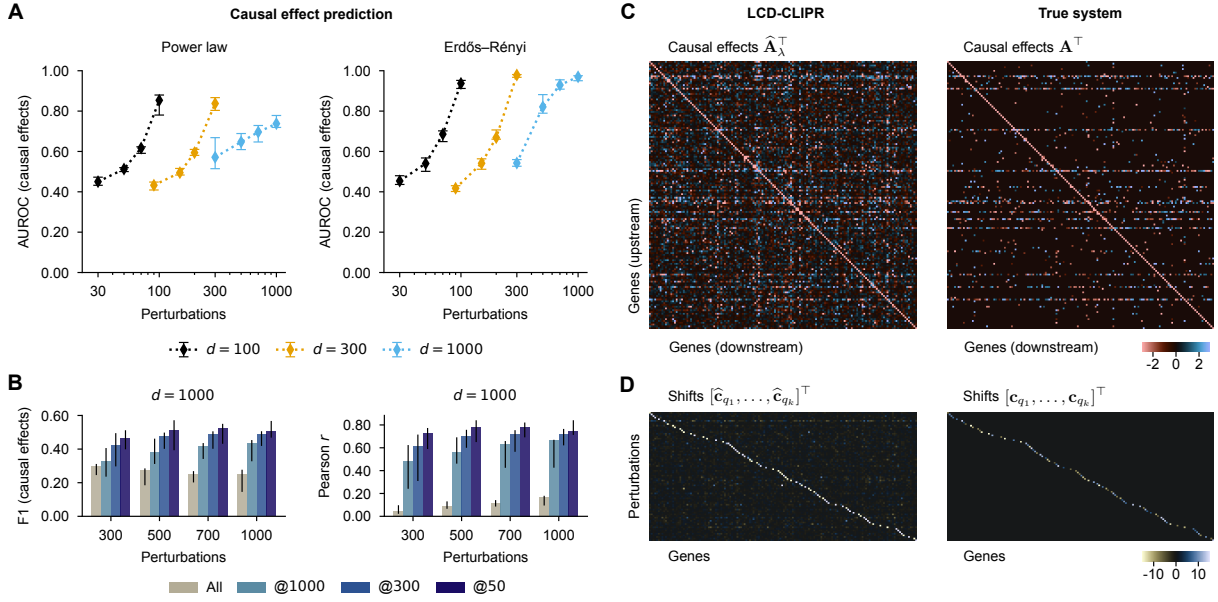


Figure 3: LCD-CLIPR accurately recovers causal effects in linear systems from learned diffusion drifts. (A) AUROC for classifying gene-gene causal effects (positive, negative, or absent) across all gene pairs. Results are shown for systems of 100, 300, and 1000 genes across varying training perturbation counts (x -axis), comparing power-law (left) and Erdős-Rényi (right) regulatory dependencies in A. (B) F1 score for classifying gene-gene causal effects (left) and average Pearson correlation between predicted and true causal effects (right) for the top k predicted effects, ranked by absolute magnitude, under power-law dependencies. Markers indicate medians, error bars indicate 10–90th percentiles across test systems. (C) Comparison of causal effects inferred by LCD-CLIPR vs. the ground-truth data-generating system (300 genes). (D) Inferred and true perturbation vectors for the system shown in C. For visual clarity, only 80 perturbations and 150 genes with the largest outgoing effects are displayed.

Combinations of gene perturbations may behave differently than their individual components suggest. We followed Norman et al. (4) and classified double-gene perturbations into six genetic interaction (GI) types based on their observed transcriptomic profiles, stratifying the performance of LCDs by GI type (SI Appendix). By comparing to the naïve additive SALT heuristic, we isolated the GI types for which LCD yielded significant improvement (Fig. 2D). LCDs improved most over an additive model, for example, for unexpected (neomorphic) GIs, where a linear model of the individual effects does not provide a good fit for the combination profile. By contrast, SALT performed on par with LCDs for redundant or epistatic GIs, where either both or one of the individual perturbations, respectively, strongly explain the combined effect. While both methods use additivity to model combinations, they differ in where this addition occurs: SALT naïvely sums differential expression profiles, whereas LCD sums perturbation embeddings \mathbf{e}_q that modulate the hidden state of a nonlinear drift function (Fig. 1A and B). This allows LCDs to capture interaction effects that unroll through the nonlinear dynamics. Fig. 2E illustrates the LCD prediction on a two-gene perturbation combination with established GI that was not seen during training (49). LCD correctly predicted most observed DE trends, both of the on-target and marker (top 20 DE) genes. SI Appendix, Fig. S2 provides additional plots for the other GI types.

Recovering causal effects in simulated systems

Next, we evaluated the CLIPR estimator component of our model. A quantitative evaluation of causal effect predictions is challenging, because the ground-truth links in gene networks are not generally known. To enable an accurate validation, we first tested CLIPR on perturbation data simulated by linear systems with single-gene shift perturbations (Eq. 3), where the true causal structure and perturbation effects are known (Methods). Here, we omitted the measurement model component of LCDs (Eq. 2) and directly trained the neural network drift f on samples of the linear systems to validate the causal structure component in isolation. Our evaluation covered ground-truth systems with varying numbers of genes and perturbed genes as well as regulatory structures in A, testing ten randomly-generated systems for each setting. We measured accuracy by classifying the gene-gene causal effects \mathbf{A}_λ predicted by CLIPR into positive, negative, or absent and then computing the area under a (three-class) receiver operating

characteristic curve (AUROC) given the ground-truth \mathbf{A} (Methods). We also tested how the predicted effect strength of $\hat{\mathbf{A}}_\lambda$ influences accuracy by computing Pearson correlations of predicted and true effects as well as F1 classification scores for the top k (@ k) predicted effects by absolute value. We use LCD-CLIPR to denote the linear causal effects estimated by applying CLIPR to the learned LCD drifts.

LCD-CLIPR achieved high accuracy in predicting both causal links and their effect signs across all sparsity structures, numbers of genes, and numbers of perturbations (Fig. 3A). The classification accuracy of LCD-CLIPR effects monotonically improved with the number of perturbations, reaching median AUROC values between 0.74–0.84 (power-law structures) and 0.93–0.98 (Erdős-Rényi structures) when observing d perturbations. Moreover, stronger predicted effects resulted in higher F1 scores and correlations with the ground truth (Fig. 3B), indicating that the strongest perturbation effects learned by the LCD drift f_g aligned strongly with those of the true system. We later build on this finding when applying LCD-CLIPR to a genome-wide Perturb-seq screen.

Fig. 3C depicts the CLIPR effects extracted from a LCD drift alongside those of the true data-generating system. LCD-CLIPR correctly identified key regulator genes of the power-law regulatory structure, visible as horizontal non-zero lines with many effects. The stability-inducing negative diagonal is recovered accurately, but LCD-CLIPR tends to be less sparse, since the estimator minimizes an ℓ^2 norm (Theorem 1). Fig. 3D shows the predicted and true shift vectors that generated the perturbation data. The CLIPR shift predictions $\hat{\mathbf{c}}_q$ follow directly from the matrix $\hat{\mathbf{A}}$ (Corollary 2). The estimator precisely recovered the single-gene targets, the on-target perturbation effects, and the near-zero off-target effects. The shifts $\hat{\mathbf{c}}_q$ were not constrained to be sparse or one-hot, but recovered the perturbation pattern solely from the inferred effects $\hat{\mathbf{A}}_\lambda$.

Disentangling causation from differential expression in Perturb-seq

Our results suggest that LCDs accurately predict perturbation responses and recover the regulatory structure of testable linear systems. We therefore reasoned that LCD-CLIPR, now including the measurement model, can be used to infer *direct* causal effects among genes in Perturb-seq screens. This capability addresses a fundamental limitation of standard differential expression analyses, which capture only *total* causal effects accumulated through the regulatory network. This distinction matters: downstream expression changes may be mediated via intermediate transcription factors or signaling pathways rather than arising from direct regulation by the perturbed gene. While perturbing gene a may cause differential expression of gene b when a directly regulates b , the converse does not hold. Differential expression does not imply direct regulation, as the effect may be propagated through intermediate genes. Understanding cellular regulatory programs therefore requires mapping direct causal mechanisms, not merely their downstream cascades.

We evaluated the capability of inferring the causal structure of direct gene-gene effects by training a LCD on a genome-wide Perturb-seq assay of the human chronic myeloid leukemia (K562) cell line (1). This screen recorded single-gene perturbations of *all* genes modeled by the LCD, providing significantly more perturbation responses for CLIPR to estimate regulatory structure compared to the combinations datasets used for benchmarking (Fig. 2; SI Appendix, Table S1). While the perturbation dynamics learned by the LCD drift f are likely highly nonlinear, our goal is to study the degree to which the linearized CLIPR causal effects predict plausible biological structure.

After estimating the CLIPR matrix $\hat{\mathbf{A}}_\lambda$ from the learned drift, we first performed hierarchical clustering of genes in the causal graph to study its network structure. We grouped genes into clusters with strong average within-cluster causal effects (Methods). To assess whether these clusters aligned with established biological annotations, we performed gene set enrichment analysis (GSEA) (50) using known ontology terms and canonical pathways (51) (Fig. 4A). Several clusters showed significant enrichment for both gene ontology terms and pathways (one-sided Fisher's exact test, $P < 0.01$, with Benjamini-Hochberg (BH) correction for multiple testing across gene clusters and annotations (52)). Moreover, clusters were enriched for distinct terms and pathways, suggesting that tight dependencies in the LCD-CLIPR graph organize genes into functionally coherent modules. Fig. 4B shows the predicted causal effects $\hat{\mathbf{A}}_\lambda$ of the genes in the clusters analyzed for enrichment. This matrix is qualitatively different than the genome-wide DE matrix (Fig. 4C, left) when ordering the perturbed genes alongside the cause (upstream) genes. Instead, the LCD-CLIPR component \mathbf{L} closely matches the differential expressions (Fig. 4C, right), since it captures

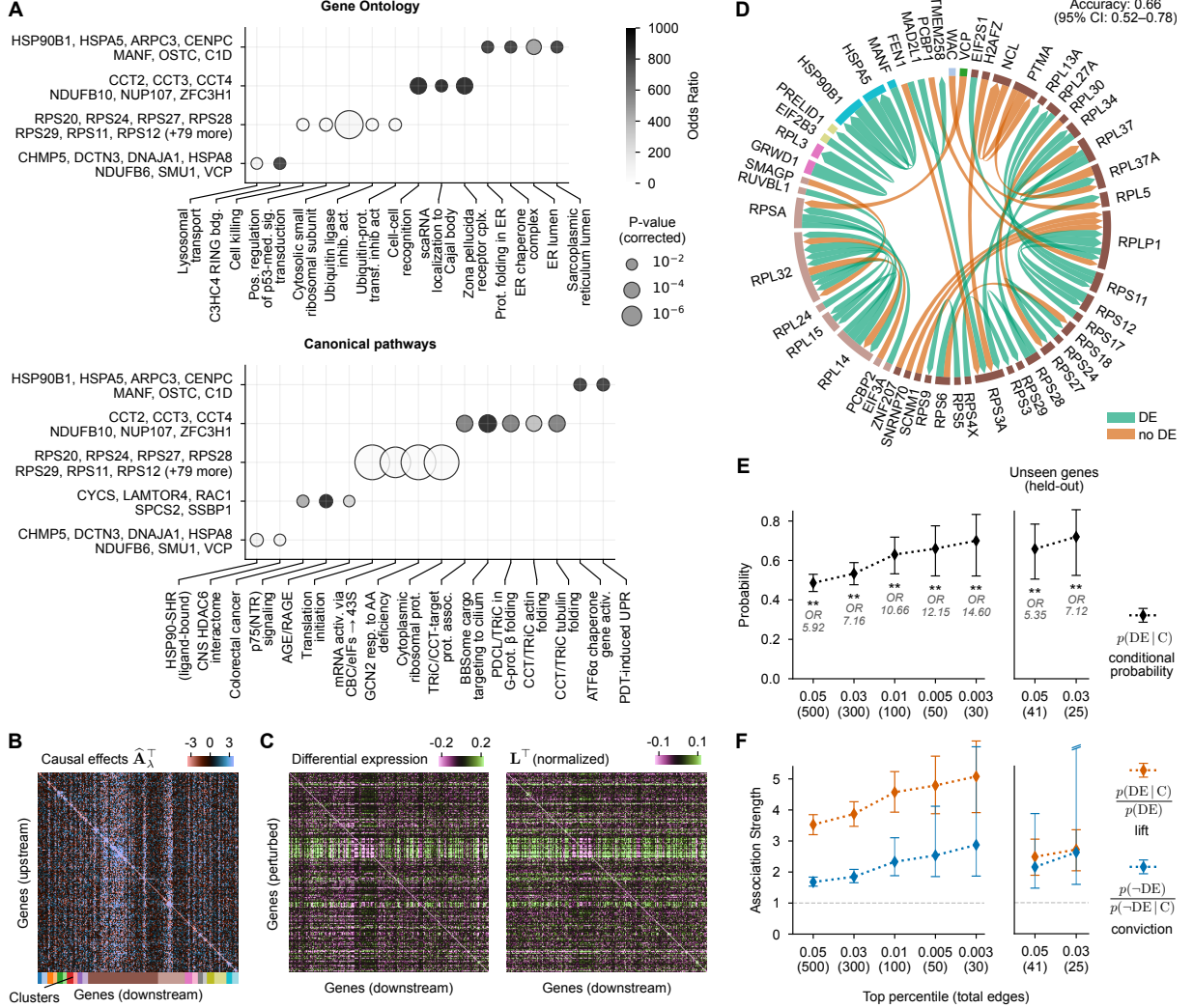


Figure 4: LCD-CLIPR infers direct gene-gene causal effects from genome-wide Perturb-seq data. (A) Hierarchical clustering based on shortest-path distances in the CLIPR graph identifies gene modules enriched for specific Gene Ontology terms (top) and canonical pathways (bottom). Clusters with at least one enriched term are shown. **(B)** Predicted causal effects and associated clusters from the enrichment analysis. **(C)** Comparison between observed differential expression (DE) (left) and normalized \mathbf{L}^+ (right). For visual clarity, only the 247 genes within identified clusters and their perturbations are shown; see SI Appendix, Fig. S5 and S6 for full matrices. **(D)** Strongest predicted causal effects (50 total). Edges are colored green where the predicted effect is validated by observed DE, and red otherwise. **(E and F)** Validation of inferred causal links (C) as a function of predicted effect strength. Stronger predicted causation significantly increases the probability of observing DE (one-sided Fisher's exact test, $P < 0.01$, OR: odds ratio). Results shown for all genes (left) and held-out genes not perturbed during training (right). Error bars indicate 95% CIs (Wilson binomial for **E**, bootstrap for **F**).

the difference in the pre- and post-perturbation equilibria (Fig. 1C). Moreover, causal effects are, as expected, sparser than differential expressions when considering all $d = 1000$ genes. We provide plots of the full matrices, including \mathbf{V} , \mathbf{L} , and \mathbf{L}^+ , in SI Appendix, Fig. S5 and S6.

Next, we validated the directed links predicted by LCD-CLIPR. In the absence of ground-truth annotations, our goal was to evaluate whether the implication discussed above—gene a directly regulating gene b implying DE of gene b when perturbing gene a —holds for the CLIPR estimates in the Perturb-seq screen, as this implication can be assessed directly from the observed data. Specifically, we studied how often this relationship holds as a function of the predicted effect strength, motivated by the observation that LCD-CLIPR was most accurate for stronger predicted effects in simulated systems (Fig. 3B). Fig. 4D shows the 50 strongest predicted causal effects (top 0.005 percentile of edges), many of which involved ribosomal protein (RP) genes, and whether a perturbation of the upstream gene caused significant DE downstream (Mann-Whitney U Test, $P < 0.05$, BH corrected for multiple testing across genes). To

quantify significance of the implication, we computed the conditional probability of DE given predicted causal dependence (C) as well as *lift* and *conviction* (53). Lift measures the likelihood of DE given C compared to DE unconditionally, and conviction quantifies how much less likely an implication violation (C but not DE) is given C. Similar to our results on simulated systems (Fig. 3B), stronger effects predicted by LCD-CLIPR significantly increased the probability of observing DE upon perturbation of the cause (Fisher’s exact test, one-sided, $P < 0.01$) (Fig. 4E, left). For the 50 strongest predicted causal effects, observing significant DE was approximately $4.78 \times$ more likely as measured by lift, and observing no DE $2.53 \times$ less likely as measured by conviction, relative to the baseline DE rates (Fig. 4F, left), suggesting that strong LCD-CLIPR links are consistent with the observed downstream effects.

CLIPR estimates a full causal structure $\hat{\mathbf{A}}_\lambda$ irrespective of whether all or only some genes were perturbed. Hence, LCD-CLIPR makes predictions about the causal effects of genes *not* originally perturbed in the screen (Fig. 3). To test this generalization capability, we split the 41 upstream genes shown in Fig. 4D (all genes identified as causes among the top 50 strongest predictions) into five test folds and trained new LCD models, each leaving out perturbations for one fold. We then applied CLIPR to each learned drift, re-aggregated the predicted causal effects for all held-out genes, and computed the previous implication metrics using the true held-out perturbation data. Without observing any on-target perturbations, the strongest LCD-CLIPR effects predicted for the held-out genes still significantly increased the probability of observing DE when perturbing the cause gene, similar to when on-target perturbations were observed (Fig. 4E, right). Significant DE was approximately $2.71 \times$ more likely, and no DE $2.62 \times$ less likely, relative to baseline DE rates for top 0.03 percentile of predicted edges (25 total) (Fig. 4F, right).

Overall, our findings suggest that LCD-CLIPR can learn biologically plausible causal structure among genes, even when genes were not perturbed in the original screen. Despite only approximating the perturbation behavior of the LCD drift, CLIPR organized genes into coherent functional clusters with tight causal effects and made meaningful predictions about which genes are affected by perturbations. This highlights two main distinguishing factors between CLIPR and DE analysis: CLIPR infers direct causal effects, DE only causal descendants; and CLIPR can generalize to genes not perturbed in the original Perturb-seq assay.

Discussion

Latent causal diffusions were designed to address the need for perturbation models that are both predictive and interpretable (3, 7, 8). As fundamentally *causal* models, they learn explicit, stochastic regulatory dynamics from Perturb-seq count inputs, assuming a principled measurement model. Perturbations modify the hidden states of the regulatory diffusion dynamics, and CLIPR enables interpreting these perturbed dynamics by constructing a linear approximation of the gene-gene causal structure of the entire system. LCDs and CLIPR thus stand in contrast to state-of-the-art deep learning approaches, which are often black-box, deterministic, or based on prior gene relationship annotations (15, 17–20, 38).

Multiple temporal trajectories can generate the same aggregate population snapshots, so inference of causal dependencies from single-cell data has fundamental limits (21). Our approach alleviates this by learning from multiple snapshots, each modeled as a perturbation of the same causal regulatory dynamics. Our results suggest that these learned dynamics often predict the outcomes of unseen perturbations more accurately than existing approaches (Fig. 2B), while recovering causal dependencies consistent with ground-truth effects of simulated systems (Fig. 3) as well as known biology (Fig. 4). Theorem 1 shows that snapshots of sufficiently diverse experimental conditions can provably identify causality, aligned with similar results showing that interventions improve identifiability (54–56).

The LCD model and CLIPR have potential limitations. In our experiments, LCDs performed best at predicting perturbation effects when the GI of a perturbation combination is unexpected, synergistic, or suppressive (Fig. 2D). When GI is additive or mean predictions suffice, simpler methods like SALT or PEPER (13), which are less computationally intensive, perform competitively. Similar to CPA, the LCD perturbation model relies on embeddings learned during training and thus only allows predicting the outcomes of combinations of observed perturbations (Fig. 1B). However, as Perturb-seq now covers the full space of individual gene perturbations (1, 2), modeling their exponential number of combinations remains the key computational challenge, which LCDs enable us to do. Beyond discovering GIs, combinations

are central to, for example, cell reprogramming (57) and drug combination therapies (58). Nonetheless, LCD-CLIPR predicted nontrivial causal structure even for unperturbed genes (Fig. 3 and Fig. 4E and F, right), showing that LCDs can make inferences about unperturbed components of the system. Ultimately, CLIPR remains a linear approximation of the learned LCD drift and likely the true regulatory dynamics, which should be taken into account when interpreting the presence or absence of specific links. This may explain why larger LCD-CLIPR effects tend to be more aligned with differential expression (Fig. 3B and Fig. 4E and F).

Finally, LCDs and CLIPR have the prospect of integrating with different biological modalities and future modeling approaches. We focused on gene perturbations to emphasize the difference between causality and differential expression, but our framework directly extends to drug perturbation screens (59), since perturbation targets need not be known to learn LCDs or compute CLIPR. Multiple batches or cell types may be integrated by conditioning the regulatory mechanisms on additional learned embeddings (Fig. 1B), similar to foundation model approaches (15). Moreover, our method for inferring state densities from counts could extend to chromatin accessibility, surface protein readouts, or beyond transcriptomics. Conversely, LCD drifts could be trained from gene states inferred by other denoising techniques (60). CLIPR could render the causal structure of any diffusion interpretable, provided it models perturbations, and therefore both LCDs and CLIPR may be of interest even outside of biology. More generally, future research could explore approaches for merging the state density and drift inference steps without dropping established noise model assumptions or the separation of biological and measurement noise (Fig. 1A). Implementing these integrations would require calibrating assumptions made by various components and careful benchmarking with existing techniques. Overall, stationary diffusions hold promise to complement Perturb-seq screens with accurate learning-based prediction and to navigate the experimental design space by improving our causal understanding of the systems we assay.

Methods

Inference

We first describe how to infer the generative model from data. We model the discrete data distributions $p(\mathbf{y})$ as noisy observations of the stationary diffusion densities $p(\mathbf{x})$, sampled by the likelihood $p(\mathbf{y} | \mathbf{x}; \boldsymbol{\pi})$. Existing techniques for learning diffusions do not separate biological (diffusion) and measurement (technical) noise we distinguish here, so we infer the generative model in two steps (Fig. 1A). Suppose we observe data $\mathbf{Y}_q = \{\mathbf{y}^{(n)}\}$ for a control condition q_0 and k perturbations q_1, \dots, q_k . Inference then proceeds in two consecutive steps (Fig. 1A):

1. Learn likelihood parameters $\boldsymbol{\pi}$ and state densities $p_q(\mathbf{x})$ that maximize evidence of the observed \mathbf{Y}_q .
Input: data \mathbf{Y}_q for each condition q
Output: $\boldsymbol{\pi}$ and samples $\mathbf{X}_q \sim p_q(\mathbf{x})$
2. Learn drift f and embeddings \mathbf{e}_q that jointly fit $p_q(\mathbf{x})$.
Input: states \mathbf{X}_q for each condition q
Output: f and embeddings \mathbf{e}_q

After both inference steps, we have learned the stationary diffusion drift f , perturbation embeddings \mathbf{e}_q , and measurement noise parameters $\boldsymbol{\pi}$. Together, these specify the full generative model and enable data generation under unseen embeddings $\mathbf{e}_{q'}$. The samples \mathbf{X}_q are only used for fitting the drift (step 2) and discarded afterwards. We now describe each step in more detail.

Measurement model Inference of the state density $p(\mathbf{x})$ corresponds to learning the *prior* that generates the data distribution $p(\mathbf{y})$, an approach called empirical Bayes (61). Our goal is not posterior inference of $p(\mathbf{x} | \mathbf{y})$, since we do not require the state that generated a specific datum \mathbf{y} . Our approach to this inference problem is to model the prior $p(\mathbf{x})$ as an implicit distribution that is easy to sample from and differentiate (62). Specifically, we model prior samples $\mathbf{x} \sim p(\mathbf{x}; \phi)$ as $\mathbf{x} = g(\boldsymbol{\epsilon}, \phi)$, where $\boldsymbol{\epsilon}$ is random noise and g a differentiable function with respect to parameters ϕ . This choice enables a flexible distributional family for $p(\mathbf{x})$ to avoid biasing the drift trained on the inferred priors in the second inference step. Implicitly

modeling the prior is possible, because both of our inference steps only require samples $\mathbf{x} \sim p(\mathbf{x}; \phi)$ or differentiating them with respect to ϕ .

We infer the prior $p(\mathbf{x}; \phi_q)$ of a condition q by maximizing the evidence of the observed readouts \mathbf{Y}_q . We use separate parameters ϕ_q for each condition q but share the likelihood parameters $\boldsymbol{\pi}$, as $\boldsymbol{\pi}$ is used for test-time generation. The evidence $\mathcal{Z}(\mathbf{Y}_q, \phi_q, \boldsymbol{\pi}) = \log p(\mathbf{Y}_q; \phi_q, \boldsymbol{\pi})$ is given by

$$\begin{aligned} \mathcal{Z}(\mathbf{Y}_q; \phi_q, \boldsymbol{\pi}) &= \sum_n \log \int p(\mathbf{x}; \phi_q) p(\mathbf{y}^{(n)} | \mathbf{x}; \boldsymbol{\pi}) d\mathbf{x} \\ &\approx \sum_n \text{LSE}_m \left\{ \log p(\mathbf{y}^{(n)} | \mathbf{x}^{(m)}; \boldsymbol{\pi}) \right\} - \log M, \end{aligned} \quad (9)$$

where we approximate the integral with M samples $\mathbf{x}^{(m)} \sim p(\mathbf{x}; \phi_q)$, written with the log-sum-exp operator $\text{LSE}_m \{z^{(m)}\} := \log \sum_m \exp(z^{(m)})$, which has a numerically stable implementation. The ZIP likelihood factors as $p(y_g | x_g; \pi_g) = \pi_g \mathbb{I}(y_g = 0) + (1 - \pi_g) \text{Pois}(y_g; \mu_g(x_g))$, where $\mathbb{I}(y_g = 0) = 1$ iff $y_g = 0$ (Eq. 2). To account for scale differences across genes, we used the rate function $\mu_g(x_g) = \eta_g \log(1 + e^{x_g})$, where η_g is a fixed gene scaling computed from control samples (see [Training Details](#)).

Optimization of \mathcal{Z} is nontrivial, since the estimator (Eq. 9) is biased and high-variance. Expanding $\log p(\mathbf{y} | \mathbf{x}; \boldsymbol{\pi}) = \sum_{g=1}^d \log p(y_g | x_g; \pi_g)$ shows that the joint likelihood inside the log-sum-exp scales linearly with d . Due to the exponential, maximizing the log-sum-exp term requires learning to generate samples with high likelihood across all d dimensions jointly, which becomes exponentially less efficient with d . We tackle this by using large M and introducing a scaling τ^{-1} of $\log p(\mathbf{y} | \mathbf{x}; \boldsymbol{\pi})$ in the loss:

$$\widehat{\mathcal{Z}}_\tau(\mathbf{Y}_q, \phi_q, \boldsymbol{\pi}) := \sum_n \tau \text{LSE}_m \left\{ \tau^{-1} \log p(\mathbf{y}^{(n)} | \mathbf{x}^{(m)}; \boldsymbol{\pi}) \right\}. \quad (10)$$

The temperature τ interpolates between fitting the full joint distribution including higher-order dependencies ($\tau = 1$, higher variance) and fitting the marginal distributions only (high τ , lower variance). As $\tau \rightarrow \infty$, the log-sum-exp operator converges to the arithmetic mean, effectively swapping logarithm and summation like a Jensen's lower bound, and treating the d dimensions in the joint likelihood as (unconditionally) independent, thus alleviating the variance caused by the exponential. Our final training objective \mathcal{L}_{IP} for learning the implicit prior is to minimize the combined loss

$$\mathcal{L}_{\text{IP}} = -\widehat{\mathcal{Z}}_1 - \widehat{\mathcal{Z}}_\tau \quad (11)$$

tuned over $\tau \in \{5, 20, 100\}$. \mathcal{L}_{IP} is fully differentiable with respect to ϕ and $\boldsymbol{\pi}$ by propagating gradients through the implicit samples $\mathbf{x} = g(\boldsymbol{\epsilon}, \phi)$.

Stationary diffusion Inferring the drift f and perturbation embeddings \mathbf{e}_q requires learning a stationary diffusion model that jointly fits the densities $p_q(\mathbf{x})$ obtained in step 1. Any learning approach may in principle be used for this. In our experiments on SDEs with constant σ (Eq. 1), score matching was computationally efficient and achieved good fit and generalization. In this setting, a drift can be inferred by denoising smoothed data $\tilde{\mathbf{x}} \sim \mathcal{N}(\tilde{\mathbf{x}}; \mathbf{x}, \alpha^2 \mathbf{I})$, where $\mathbf{x} \sim p(\mathbf{x})$. The drift f that minimizes the squared loss $\|f(\tilde{\mathbf{x}}) + (\tilde{\mathbf{x}} - \mathbf{x})/\alpha^2\|_2^2$ in expectation satisfies $f(\tilde{\mathbf{x}}) = \nabla \log p(\tilde{\mathbf{x}}; \alpha)$ under weak regularity conditions, which implies the SDE has stationary density $p(\tilde{\mathbf{x}}; \alpha)$ for $\sigma = \sqrt{2}$ (63). The difference between $\nabla \log p(\tilde{\mathbf{x}}; \alpha)$ and $\nabla \log p(\mathbf{x})$ becomes negligible as $\alpha \rightarrow 0$. Following Song and Ermon (64), we thus infer f by learning to denoise different smoothing levels α , conditioning the drift on α . The loss for drift $f(\mathbf{x}; \theta, \mathbf{e}_q, \alpha)$ is then

$$\mathcal{L}_{\text{D}}(\mathbf{X}_q, \theta, \mathbf{e}_q, \alpha^{(n)}) = \sum \|\alpha^{(n)} f(\tilde{\mathbf{x}}^{(n)}; \theta, \mathbf{e}_q, \alpha^{(n)}) + \boldsymbol{\epsilon}^{(n)}\|_2^2 \quad (12)$$

where $\tilde{\mathbf{x}}^{(n)} = \mathbf{x}^{(n)} + \alpha^{(n)} \boldsymbol{\epsilon}^{(n)}$, $\boldsymbol{\epsilon}^{(n)} \sim \mathcal{N}(\mathbf{0}, \mathbf{I}_d)$, and the scales $\alpha^{(n)}$ are drawn from the geometric sequence $\boldsymbol{\alpha} = [0.01, \dots, 10] \in \mathbb{R}^{30}$. In Eq. 12, we scaled the norm by α^2 to ensure that loss terms have comparable magnitudes. Training on multiple and large smoothing levels α avoided a behavior we called ‘multi-fitting’: without higher smoothing scales α , diffusions tended to fit all perturbed densities $p_q(\mathbf{x})$ unconditionally like a mixture distribution of all conditions, ignoring the embeddings \mathbf{e}_q . Avoiding this also required careful sampling based on $\boldsymbol{\alpha}$ (see [Sampling](#)). For CLIPR, we condition f on the smallest $\alpha_1 = 0.01$ and

thus least smoothing error (see CLIPR). We fixed the diffusion scale σ (Eq. 1) to $\sigma = \sqrt{2}$ throughout all experiments and shared θ across conditions q , modeling the gene regulatory mechanisms and enabling test-time generation for unseen \mathbf{e}_q .

Score matching fits the drift $f(\mathbf{x}; \theta, \mathbf{e}_q)$ to a gradient field, abstracting away the fact that θ is fit to multiple densities and coupled through \mathbf{e}_q . While this would imply that steady-state dynamics have zero curl ($\partial[f_q]_a / \partial x_b = \partial[f_q]_b / \partial x_a$), the perturbation behavior modeled by LCDs is not symmetric. Because perturbations modify the hidden state of a nonlinear drift (Fig. 1B), perturbing gene a may not have the same effect on gene b as perturbing gene b has on gene a . CLIPR reveals that LCD perturbations indeed exhibit asymmetry (Fig. 3C and Fig. 4B). To learn stationary densities with non-zero curl and enable modeling, for example, negative feedback loops of three repressors (21, 34), future work could leverage more general learning objectives not based on the gradient field assumption (29).

Sampling

To generate data $\mathbf{y} \sim p_q(\mathbf{y})$ for a test perturbation \mathbf{e}_q , we conditioned f on the test embedding \mathbf{e}_q and simulated the diffusion to obtain samples $\mathbf{x} \sim p_q(\mathbf{x})$ from the stationary density. For a perturbation combination of q_a and q_b , the embedding is $\mathbf{e}_{q_a} + \mathbf{e}_{q_b}$ (see [Neural network architectures](#)). We generated diffusion samples by annealing the Euler-Maruyama method according to the trained smoothing levels α (64). The sample path approximation at step l is (65)

$$\mathbf{x}^{(l+1)} = \mathbf{x}^{(l)} + f(\mathbf{x}^{(l)}; \theta, \mathbf{e}_q, \alpha^{(l)})(\alpha^{(l)})^2 \Delta t + \boldsymbol{\xi}^{(l)} \alpha^{(l)} \sqrt{2\Delta t} \quad (13)$$

for noise $\boldsymbol{\xi}^{(l)} \sim \mathcal{N}(\mathbf{0}, \mathbf{I}_d)$, step size Δt , and smoothing level $\alpha^{(l)}$. In our experiments, we used $\Delta t = 10^{-4}$, initialized at $\mathbf{x}(0) \sim \mathcal{N}(\mathbf{0}, \mathbf{I}_d)$, and computed 500 Euler-Maruyama steps per annealing scale in $\boldsymbol{\alpha}$, starting with $\alpha_{30} = 10.0$ and ending at $\alpha_1 = 0.01$. The last state $\mathbf{x}^{(l)}$ corresponds to the sample from $p_q(\mathbf{x})$ after inverting the shift and scale standardization performed on the training data (see [Training details](#)). For each $\mathbf{x} \sim p_q(\mathbf{x})$, we generated one observation $\mathbf{y} \sim p(\mathbf{y} | \mathbf{x}; \boldsymbol{\pi})$ (Eq. 2) as the final sample from the LCD.

Neural network architectures

For our experiments, we parameterized the drift and the implicit priors using multi-layer perceptrons (MLPs). The implicit prior network $g(\boldsymbol{\epsilon}, \phi)$ transformed noise $\boldsymbol{\epsilon} \sim \mathcal{N}(\boldsymbol{\epsilon}; \mathbf{0}, \mathbf{I}_{64}) \in \mathbb{R}^{64}$ into samples $\mathbf{x} = g(\boldsymbol{\epsilon}, \phi) \in \mathbb{R}^d$. After an initial linear layer mapping $\boldsymbol{\epsilon}$ to 64 dimensions, the network consisted of a sequence of residual MLP blocks with 64 hidden dimensions (4 blocks), followed by a linear layer mapping to d dimensions, and additional residual MLP layers with 256 hidden dimensions (2 blocks). Residual MLP blocks computed output \mathbf{z}' from input \mathbf{z} as $\mathbf{z}' := \mathbf{z} + \text{Linear}(\text{SiLU}(\text{Linear}(\mathbf{z})))$, where $\text{SiLU}(\mathbf{z}) := \mathbf{z} * \text{sigmoid}(\mathbf{z})$ elementwise and $\text{Linear}(\mathbf{z}) := \mathbf{W}\mathbf{z} + \mathbf{b}$ with independent parameters \mathbf{W}, \mathbf{b} and corresponding dimensions per layer. Residual layers stabilized training and the variance of $p(\mathbf{x}; \phi)$, and the low dimensionality reduced memory, enabling larger Monte Carlo sample sizes M during training.

The drift $f(\mathbf{x}; \theta, \mathbf{e}_q, \alpha)$ was parameterized by a fixed α -dependent scaling to adjust for changing state and gradient magnitudes across the different smoothing scales α (66). Specifically, we modeled f as

$$f(\mathbf{x}; \theta, \mathbf{e}_q, \alpha) = \frac{1}{\alpha} h\left(\frac{\mathbf{x}}{\sqrt{1 + \alpha^2}}; \theta, \mathbf{e}_q, \alpha\right) \quad (14)$$

where h is the main neural network parameterized by θ , taking state \mathbf{x} , perturbation embedding \mathbf{e}_q , and smoothing scale α as input. h is an MLP with two hidden layers, tanh nonlinearities, and $d_f \in \{1024, 2048\}$ dimensions (Fig. 1B). Representations \mathbf{e}_q have 1024 dimensions and are jointly learned with θ . They are added to both hidden states of the MLP before the nonlinearity following separate learned linear transformations, similar to conditioning techniques in vision models (67). We model combinations of perturbations q_a and q_b by adding embeddings as $\mathbf{e}_{q_a, q_b} = \mathbf{e}_{q_a} + \mathbf{e}_{q_b}$ and represent the control condition q_0 by the zero vector $\mathbf{e}_{q_0} = \mathbf{0}$. Lastly, h models the effect of α by encoding the index of α in the sequence $\boldsymbol{\alpha}$ as a sinusoidal position embedding (68), then mapping to d_f dimensions with a linear layer, tanh nonlinearity, and a second linear layer, and finally adding the α representation to the first hidden state of h .

Training details

As described in [Inference](#), we observe data \mathbf{Y}_q for a control condition q_0 and k perturbations q_1, \dots, q_k . Training then proceeds in two consecutive steps. We used the same training hyperparameters devised during development of the method across all experiments unless we note they are tuned otherwise (see [Baselines and hyperparameters](#)).

We learned the priors by minimizing \mathcal{L}_{IP} (Eq. 11) with gradient descent for 250,000 steps. We used the Adam optimizer (69) ($\beta_1 = 0$, $\beta_2 = 0.99$) with learning rate 0.0003, warmed up for 5000 steps and cosine-decayed to zero. Each step randomly sampled a perturbation q and then updated parameters ϕ_q and $\boldsymbol{\pi}$ based on \mathbf{Y}_q . The loss \mathcal{L}_{IP} was computed using a batch size of 64 and $M = 20,000$ Monte Carlo samples. Gradients were clipped at ℓ_2 -norm 1.0. We fixed the gene-specific scalings in the Poisson rate $\mu_g(x_g)$ (Eq. 2) to $\eta_g = \bar{y}_g + \bar{s}_g^2/\bar{y}_g - 1$, lower bounded by 1, where \bar{y}_g and \bar{s}_g^2 are sample means and variances of y_g in the control data \mathbf{Y}_{q_0} . This is the method-of-moments estimator for the Poisson mean under a ZIP model of y_g (70) and thus calibrated $\mu_g(x_g)$ to the expected scale of y_g . Training the implicit priors did not overfit, since the Poisson has a minimum level of dispersion, and therefore training did not include explicit regularization. We validated model fit by tracking the evidence \mathcal{Z} and comparing generated samples to \mathbf{Y}_q after passing them through the learned likelihood. After optimization, we generated $N = 10,000$ state samples $\mathbf{X}_q = \{\mathbf{x}^{(n)}\}_{n=1}^N \sim p(\mathbf{x}; \phi_q)$ for training the diffusion.

We trained the drift f and perturbation embeddings \mathbf{e}_q by minimizing \mathcal{L}_{D} (Eq. 12) with gradient descent for 50,000 steps. We used the Adam optimizer ($\beta_1 = 0.9$, $\beta_2 = 0.999$) with learning rate 0.001, cosine-decayed to zero, and weight decay tuned over $\{0.03, 0.1, 0.3, 1.0, 3.0\}$. Weight decay was most effective at controlling over- and underfitting and tuning predictive performance of LCDs. As during prior inference (step 1), each update step randomly selected one condition q , one smoothing level α , and then updated parameters θ and \mathbf{e}_q , using a batch size of 8192 to compute \mathcal{L}_{D} . We standardized the training data to facilitate gradient-based optimization by subtracting the control means of \mathbf{X}_0 and dividing by the standard deviations across all training samples $\mathbf{X}_0, \dots, \mathbf{X}_k$. [SI Appendix](#) summarizes the computational requirements of training.

CLIPR

We numerically approximated the fixed point defining the perturbation response \mathbf{l}_{f_q} by integrating the flow of f conditioned on \mathbf{e}_q as

$$\mathbf{l}_{f_q} \approx \lim_{t \rightarrow \infty} \bar{\mathbf{x}}(t), \quad (15)$$

where $d\bar{\mathbf{x}}(t)/dt = f(\bar{\mathbf{x}}(t); \theta, \mathbf{e}_q, \alpha_1)$ and $\bar{\mathbf{x}}(0) = \mathbf{0}$ (Fig. 1C). For integration, we used the same annealing scheme as used for generation but dropped the noise term (see [Sampling](#)). Integration starting from the control vector $\mathbf{0}$ resolves the ambiguity that f_q may admit multiple fixed points. We assume throughout that this limit exists, which held true in all experiments. To compute CLIPR, we assembled the \mathbf{V} and \mathbf{L} matrices (Theorem 1) by conditioning the drift f separately on each perturbation embedding \mathbf{e}_q learned during training (i.e., ignoring combinations, which are modeled as sums of embeddings). We used a regularization strength of $\lambda = 1/10d$ for systems of d variables, which worked well across all settings (Figs. 3 and 4), specifically $\lambda = 10^{-3}$ for $d = 100$, $\lambda = 3 \cdot 10^{-3}$ for $d = 300$, and $\lambda = 10^{-4}$ for $d = 1000$.

We standardize the states $p(\mathbf{x})$ before learning f , so the learned f operates in different unit scales than the original $p(\mathbf{x})$ (see [Training Details](#)). However, we still want to interpret the causal effects of the drift corresponding to the original units when applying CLIPR to f learned in standardized units. Put differently, we seek the CLIPR linearization of the drift we *would have learned* had the data not be standardized. To accomplish this, additional results in [SI Appendix](#) provide the original drift f^x as an explicit function of the data transformation and learned drift f^s assuming the diffusion scale σ is fixed. We show that, if densities $p(\mathbf{x})$ are transformed such that $\mathbf{x} = \mathbf{m} + \mathbf{T}\mathbf{s}$, where $\mathbf{m} \in \mathbb{R}^d$ and $\mathbf{T} \in \mathbb{R}^{d \times d}$ is positive definite, the perturbation responses of $f^x(\mathbf{x})$ (Eqs. 5 and 6) are given in terms of $f^s(\mathbf{s})$ as

$$\begin{aligned} \mathbf{v}_{f^x} &= \mathbf{T}^{-1} f^s(-\mathbf{T}^{-1} \mathbf{m}), \\ \mathbf{l}_{f^x} &= \mathbf{m} + \mathbf{T} \mathbf{l}_{f^s}. \end{aligned} \quad (16)$$

We always applied Eq. 16 before computing CLIPR to account for data standardization before training. [SI Appendix](#) provides formal statements of these results and applies them to linear SDEs as a practical illustration.

Datasets and preprocessing

We performed experiments on Perturb-seq data by Norman et al. (4) and Wessels et al. (5) (Fig. 2) and by Replegle et al. (1) (Fig. 4). All datasets were prepared with standard preprocessing steps. Initial quality control filtered genes expressed in less than 20 cells, cells measuring less than 200 genes, and perturbations with less than 100 cells, as well as outliers based on dataset-specific cutoffs for high mitochondrial RNA counts and total cell and gene counts. For benchmarking, we split the double-gene perturbations into a validation set of 20 perturbations for hyperparameter tuning and a test set used for benchmarking, which was split further into 10 folds. For a given test fold, methods were trained on control, single-gene, and double-gene perturbations of the remaining test folds. Combining all experiments, we obtained test-time predictions for all double-gene perturbations ([SI Appendix](#), Fig. S1). [SI Appendix](#), Table S1 lists summary statistics for the perturbations available in each dataset.

For all datasets, we modeled 1000 highly variable genes based on Seurat-dispersions (71) of the control and single-gene perturbation data (always in training split), normalized to median control library sizes and \log_{10} transformed. Gene selection prioritized perturbed genes and top 20 marker genes of the perturbations. Norman et al. recorded the single-gene perturbations underlying most double-gene perturbations, which enabled us to classify gene pairs into GI categories by comparing the single and double post-perturbation means ([SI Appendix](#)). GI metrics computed on the 1000 selected genes correlated with those computed on the full gene set ([SI Appendix](#), Fig. S3). We therefore determined thresholds for GI types based on the classifications of the original study ([SI Appendix](#), Fig. S4).

We also performed experiments on perturbation data generated by linear systems (Fig. 3). For each evaluation setting, we randomly generated ten linear systems (Eq. 3) with different parameters \mathbf{A}, \mathbf{b} and then sampled single-gene perturbation data using one-sparse shift vectors \mathbf{c}_q . Specifically, we sampled $\mathbf{A} \sim \text{Unif}_{\pm}(1, 3)$ and $\mathbf{b} \sim \text{Unif}(-3, 3)$, where Unif_{\pm} denotes a uniform distribution with random signs, masked \mathbf{A} by random Erdős-Rényi and power-law sparsity structures, and then shifted the masked \mathbf{A} by a constant diagonal to ensure stability with a maximum eigenvalue of -0.5 (29). Erdős-Rényi structures contained independently-sampled non-zero entries (10 per gene in expectation) (72), and power-law structures were randomly generated with few regulator genes and many downstream genes (Barabási-Albert preferential attachment with strength 2 and 10 links per gene, orientation flipped with probability 0.1 to create feedback loops) (73). Each perturbation \mathbf{c}_q targeted a unique gene g with on-target shift $[\mathbf{c}_q]_g \sim \text{Unif}_{\pm}(5, 15)$ and zero entries otherwise. The simulated datasets contained 200 samples per perturbation.

Enrichment Analysis

We analyzed the causal structure inferred from the Perturb-seq screen (Fig. 4A) by hierarchically clustering genes based on their causal effects. Gene distances were defined as shortest path lengths in the graph $\mathbf{W}_\lambda + \mathbf{W}_\lambda^\top$, where $\mathbf{W}_\lambda = 1/|\hat{\mathbf{A}}_\lambda + 10^{-10}|$ to ensure symmetry and capture indirect dependency. We then clustered genes by iteratively linking sets with minimal average distances. We obtained the final set of tight gene clusters by cutting the dendrogram at the lowest height that still grouped ribosomal protein genes into a single cluster, which constituted a large, tight cluster upon visual inspection ([SI Appendix](#), Fig. S5). Clusters containing fewer than five genes as well as genes not assigned to any cluster after cutting the dendrogram were excluded from further analysis. We performed GSEA on the predicted gene clusters by testing for overrepresentation in gene ontology terms (C5.GO) and canonical pathways (C2.CP) of the MSigDB database (51), using one-sided Fisher's exact tests and correcting for multiple testing across both gene clusters and annotations. Fig. 4A shows top five enriched terms per predicted cluster, ranked by odds ratio. We increased the CLIPR regularization to $\lambda = 10^{-2}$ compared to the benchmarking datasets, which included either substantially fewer perturbations or no model mismatch, as the matrix $\hat{\mathbf{A}}_\lambda$ had not yet stabilized at the default $\lambda = 10^{-4}$ (see [CLIPR](#)).

Metrics

For benchmarking, each method generated 1000 samples per test perturbation (Fig. 2). We computed MMD using a squared exponential kernel $k(\mathbf{y}, \mathbf{y}') = \exp(-\|\mathbf{y} - \mathbf{y}'\|_2^2/2d\gamma^2)$, averaged over 10 length scales $\gamma \in [0.01, 10]$ in geometric progression (18). We also calculated RMSE and Pearson correlation between the predicted and observed means, respectively, aligned with previous works (17, 19). We identified the top 20 differentially expressed (marker) genes relative to control using Mann-Whitney U tests with BH correction. Metrics were computed on normalized counts (library size 10^4 , log1p transformed). An explicit definition of the empirical MMD is given in [SI Appendix](#).

For evaluating CLIPR, we computed the accuracy of $\hat{\mathbf{A}}_\lambda$ relative to the ground-truth \mathbf{A} by classifying the predicted effects into positive, negative, and absent using the thresholds ± 0.5 (Fig. 3). We reported one-versus-one AUROC scores averaged over the three class pairs, using predicted effect strength as confidences, which is insensitive to class imbalance (74). We calculated the F1 score for the three-class setting by averaging the scores predicted for each label. All metrics excluded the diagonals of the causal effect matrix (self-links).

Baselines and hyperparameters

We compared LCDs to various methods (Fig. 2). All figures show the baseline performance achieved by random control and perturbed cells of all training perturbations. SALT predicted post-perturbation effects of double perturbations as the sum of their constituent single perturbation effects (13). Specifically, let $\Delta_q \in \mathbb{R}^d$ denote the mean differential expression of the normalized and log-transformed counts after perturbation q . Then, SALT generated samples for a double perturbation q_a, q_b by shifting randomly sampled control data by $\Delta_{q_a} + \Delta_{q_b}$. If q was not observed as a single perturbation, SALT imputed the mean across all training perturbations. [SI Appendix](#) provides details on the other baselines.

We tuned loss temperature τ , hidden size d_f , and weight decay for LCDs and key hyperparameters of each baseline. For this, we selected configurations that minimized the median MMD (top 20 DE genes) evaluated on a validation split of the double-gene perturbations ([SI Appendix](#), Fig. S1). [Training Details](#) provides details for LCD and [SI Appendix](#) for the baselines. For the linear systems and genome-wide Perturb-seq and experiments (Figs. 3 and 4), we trained on significantly more perturbations and thus doubled the drift training steps. Because these datasets lack double perturbations for validation, we fixed hyperparameters at intermediate values of $\tau = 20$, weight decay = 1, and $d_f = 2048$.

Acknowledgments and Disclosure of Funding

We thank Elvira Forte, Frederike Lübeck, and Scott Sussex for helpful feedback on the manuscript. This work has also greatly benefited from discussions with Marco Bagatella, Frederike Lübeck, Matteo Pariset, Scott Sussex, Lenart Treven, and fellows of the Eric and Wendy Schmidt Center at the Broad Institute. L.L. and A.K. were partially supported by the Swiss National Science Foundation under NCCR Automation, grant agreement 51NF40 180545 and L.L. and B.S. were partially supported by the Deutsche Forschungsgemeinschaft (DFG, German Research Foundation) under Germany's Excellence Strategy – EXC number 2064/1. J.Z. was supported by the Eric and Wendy Schmidt Center at the Broad Institute. C.U. was partially supported by NCCIH/NIH (1DP2AT012345), NIDDK/NIH (5RC2DK135492-02), ONR (N00014-24-1-2687), and the United States Department of Energy (DE-SC0023187).

Author Contributions

L.L., J.Z., C.B., A.K., B.S., and C.U. designed research; L.L., J.Z., and C.B. conceived the LCD model; L.L. developed inference steps, CLIPR, software, and performed experiments; L.L., J.Z., C.B., A.K., B.S., and C.U. analyzed data and wrote the paper; A.K., B.S., and C.U. supervised the research.

Declaration of Interests

The authors declare no competing financial interests.

Data and Code Availability

All code was implemented in Python. The source code will be released upon publication of this work.

References

1. Joseph M Replogle, Reuben A Saunders, Angela N Pogson, Jeffrey A Hussmann, Alexander Lenail, Alina Guna, Lauren Mascibroda, Eric J Wagner, Karen Adelman, Gila Lithwick-Yanai, et al. Mapping information-rich genotype-phenotype landscapes with genome-scale Perturb-seq. *Cell*, 185(14):2559–2575, 2022.
2. Rebecca J Carlson, Michael D Leiken, Alina Guna, Nir Hacohen, and Paul C Blainey. A genome-wide optical pooled screen reveals regulators of cellular antiviral responses. *Proceedings of the National Academy of Sciences*, 120(16):e2210623120, 2023.
3. Jennifer E Rood, Anna Hupalowska, and Aviv Regev. Toward a foundation model of causal cell and tissue biology with a Perturbation Cell and Tissue Atlas. *Cell*, 187(17):4520–4545, 2024.
4. Thomas M Norman, Max A Horlbeck, Joseph M Replogle, Alex Y Ge, Albert Xu, Marco Jost, Luke A Gilbert, and Jonathan S Weissman. Exploring genetic interaction manifolds constructed from rich single-cell phenotypes. *Science*, 365(6455):786–793, 2019.
5. Hans-Hermann Wessels, Alejandro Méndez-Mancilla, Yuhao Hao, Efthymia Papalexi, William M Mauck III, Lu Lu, John A Morris, Eleni P Mimitou, Peter Smibert, Neville E Sanjana, et al. Efficient combinatorial targeting of RNA transcripts in single cells with Cas13 RNA Perturb-seq. *Nature methods*, 20(1):86–94, 2023.
6. Brian Cleary and Aviv Regev. The necessity and power of random, under-sampled experiments in biology. *arXiv preprint arXiv:2012.12961*, 2020.
7. Alejandro Tejada-Lapuerta, Paul Bertin, Stefan Bauer, Hananeh Aliee, Yoshua Bengio, and Fabian J Theis. Causal machine learning for single-cell genomics. *Nature Genetics*, pages 1–12, 2025.
8. Caroline Uhler. Building a two-way street between cell biology and machine learning. *Nature cell biology*, 26(1):13–14, 2024.
9. Jake P. Taylor-King, Michael Bronstein, and David Roblin. The future of machine learning within target identification: Causality, reversibility, and druggability. *Clinical Pharmacology & Therapeutics*, 115(4):655–657, 2024.
10. Daniel Dimitrov, Stefan Schrod, Martin Rohbeck, and Oliver Stegle. Interpretation, extrapolation and perturbation of single cells. *Nature Reviews Genetics*, pages 1–22, 2026.
11. George I Gavriilidis, Vasileios Vasileiou, Aspasia Orfanou, Naveed Ishaque, and Fotis Psomopoulos. A mini-review on perturbation modelling across single-cell omic modalities. *Computational and Structural Biotechnology Journal*, 23:1886, 2024.
12. Constantin Ahlmann-Eltze, Wolfgang Huber, and Simon Anders. Deep-learning-based gene perturbation effect prediction does not yet outperform simple linear baselines. *Nature Methods*, pages 1–5, 2025.
13. Thomas Gaudelet, Alice Del Vecchio, Eli M Carrami, Juliana Cudini, Chantriont-Andreas Kapourani, Caroline Uhler, and Lindsay Edwards. Season combinatorial intervention predictions with Salt & Peper. *arXiv preprint arXiv:2404.16907*, 2024.
14. Christina V Theodoris, Ling Xiao, Anant Chopra, Mark D Chaffin, Zeina R Al Sayed, Matthew C Hill, Helene Mantineo, Elizabeth M Brydon, Zexian Zeng, X Shirley Liu, et al. Transfer learning enables predictions in network biology. *Nature*, 618(7965):616–624, 2023.
15. Haotian Cui, Chloe Wang, Hassaan Maan, Kuan Pang, Fengning Luo, Nan Duan, and Bo Wang. scGPT: toward building a foundation model for single-cell multi-omics using generative AI. *Nature methods*, 21(8):1470–1480, 2024.
16. Yanay Rosen, Maria Brbić, Yusuf Roohani, Kyle Swanson, Ziang Li, and Jure Leskovec. Toward universal cell embeddings: integrating single-cell RNA-seq datasets across species with SATURN. *Nature Methods*, 21(8):1492–1500, 2024.
17. Yusuf Roohani, Kexin Huang, and Jure Leskovec. Predicting transcriptional outcomes of novel multigene perturbations with GEARS. *Nature Biotechnology*, 42(6):927–935, 2024.
18. Charlotte Bunne, Stefan G Stark, Gabriele Gut, Jacobo Sarabia Del Castillo, Mitch Levesque, Kjong-Van Lehmann, Lucas Pelkmans, Andreas Krause, and Gunnar Rätsch. Learning single-cell perturbation responses using neural optimal transport. *Nature methods*, 20(11):1759–1768, 2023.
19. Mohammad Lotfollahi, Anna Klimovskaia Susmelj, Carlo De Donno, Leon Hetzel, Yuge Ji, Ignacio L Ibarra, Sanjay R Srivatsan, Mohsen Naghipourfar, Riza M Daza, Beth Martin, et al. Predicting cellular responses to complex perturbations in high-throughput screens. *Molecular systems biology*, 19(6):e11517, 2023.
20. Chujun He, Jiaqi Zhang, Munther Dahleh, and Caroline Uhler. Morph predicts the single-cell outcome of genetic perturbations across conditions and data modalities. *bioRxiv*, 2025.

21. Caleb Weinreb, Samuel Wolock, Betsabeh K Tusi, Merav Socolovsky, and Allon M Klein. Fundamental limits on dynamic inference from single-cell snapshots. *Proceedings of the National Academy of Sciences*, 115(10):E2467–E2476, 2018.
22. Andrew E Teschendorff and Andrew P Feinberg. Statistical mechanics meets single-cell biology. *Nature Reviews Genetics*, 22(7):459–476, 2021.
23. Daniel T Gillespie. Exact stochastic simulation of coupled chemical reactions. *The journal of physical chemistry*, 81(25):2340–2361, 1977.
24. Thomas B Kepler and Timothy C Elston. Stochasticity in transcriptional regulation: origins, consequences, and mathematical representations. *Biophysical journal*, 81(6):3116–3136, 2001.
25. Arjun Raj, Charles S Peskin, Daniel Tranchina, Diana Y Vargas, and Sanjay Tyagi. Stochastic mRNA synthesis in mammalian cells. *PLoS biology*, 4(10):e309, 2006.
26. Vahid Shahrezaei and Peter S Swain. Analytical distributions for stochastic gene expression. *Proceedings of the National Academy of Sciences*, 105(45):17256–17261, 2008.
27. Romain Lopez, Jeffrey Regier, Michael B Cole, Michael I Jordan, and Nir Yosef. Deep generative modeling for single-cell transcriptomics. *Nature methods*, 15(12):1053–1058, 2018.
28. Payam Dibaenia and Saurabh Sinha. SERGIO: a single-cell expression simulator guided by gene regulatory networks. *Cell systems*, 11(3):252–271, 2020.
29. Lars Lorch, Andreas Krause, and Bernhard Schölkopf. Causal modeling with stationary diffusions. In *Proceedings of The 27th International Conference on Artificial Intelligence and Statistics*, volume 238 of *Proceedings of Machine Learning Research*, pages 1927–1935, 2024.
30. Michael B Elowitz, Arnold J Levine, Eric D Siggia, and Peter S Swain. Stochastic gene expression in a single cell. *Science*, 297(5584):1183–1186, 2002.
31. Ertugrul M Ozbudak, Mukund Thattai, Iren Kurtser, Alan D Grossman, and Alexander Van Oudenaarden. Regulation of noise in the expression of a single gene. *Nature genetics*, 31(1):69–73, 2002.
32. Bernt Øksendal. *Stochastic differential equations*. Springer, 2003.
33. René Thomas, Denis Thieffry, and Marcelle Kaufman. Dynamical behaviour of biological regulatory networks—I. Biological role of feedback loops and practical use of the concept of the loop-characteristic state. *Bulletin of mathematical biology*, 57(2):247–276, 1995.
34. Michael B Elowitz and Stanislas Leibler. A synthetic oscillatory network of transcriptional regulators. *Nature*, 403(6767):335–338, 2000.
35. Uri Alon. Network motifs: theory and experimental approaches. *Nature Reviews Genetics*, 8(6):450–461, 2007.
36. Grace Hui Ting Yeo, Sachit D Saksena, and David K Gifford. Generative modeling of single-cell time series with prescient enables prediction of cell trajectories with interventions. *Nature communications*, 12(1):3222, 2021.
37. Michael E Vinyard, Anders W Rasmussen, Ruitong Li, Allon M Klein, Gad Getz, and Luca Pinello. scDiffEq: drift-diffusion modeling of single-cell dynamics with neural stochastic differential equations. *bioRxiv*, pages 2023–12, 2023.
38. Siyu He, Yuefei Zhu, Daniel Naveed Tavakol, Haotian Ye, Yeh-Hsing Lao, Zixian Zhu, Cong Xu, Shradha Chauhan, Guy Garty, Raju Tomer, et al. Squidiff: Predicting cellular development and responses to perturbations using a diffusion model. *Nature Methods*, pages 1–13, 2025.
39. Amos Tanay, Roded Sharan, and Ron Shamir. Discovering statistically significant biclusters in gene expression data. *Bioinformatics-Oxford*, 18(1):S136, 2002.
40. Eran Segal, Michael Shapira, Aviv Regev, Dana Pe'er, David Botstein, Daphne Koller, and Nir Friedman. Module networks: identifying regulatory modules and their condition-specific regulators from gene expression data. *Nature genetics*, 34(2):166–176, 2003.
41. Mark Isalan, Caroline Lemerle, Konstantinos Michalodimitrakis, Carsten Horn, Pedro Beltrao, Emanuele Raineri, Mireia Garriga-Canut, and Luis Serrano. Evolvability and hierarchy in rewired bacterial gene networks. *Nature*, 452(7189):840–845, 2008.
42. Graham Heimberg, Rajat Bhatnagar, Hana El-Samad, and Matt Thomson. Low dimensionality in gene expression data enables the accurate extraction of transcriptional programs from shallow sequencing. *Cell systems*, 2(4):239–250, 2016.
43. Timothy R Hughes, Matthew J Marton, Allan R Jones, Christopher J Roberts, Roland Stoughton, Christopher D Armour, Holly A Bennett, Ernest Coffey, Hongyue Dai, Yudong D He, et al. Functional discovery via a compendium of expression profiles. *Cell*, 102(1):109–126, 2000.
44. Dominic Grün, Lennart Kester, and Alexander Van Oudenaarden. Validation of noise models for single-cell transcriptomics. *Nature methods*, 11(6):637–640, 2014.
45. Martin Jacobsen. A brief account of the theory of homogeneous Gaussian diffusions in finite dimensions. *Frontiers in Pure and Applied Probability* 1, 1993.
46. Joris M Mooij, Jonas Peters, Dominik Janzing, Jakob Zscheischler, and Bernhard Schölkopf. Distinguishing cause from effect using observational data: methods and benchmarks. *Journal of Machine Learning Research*, 17(32):1–102, 2016.
47. Lanxiang Li, Yue You, Yunlin Fu, Wenyu Liao, Xueying Fan, Shihong Lu, Ye Cao, Bo Li, Wenle Ren, Jiaming Kong, et al. A systematic comparison of single-cell perturbation response prediction models. *bioRxiv*, pages 2024–12, 2024.

48. Arthur Gretton, Karsten M Borgwardt, Malte J Rasch, Bernhard Schölkopf, and Alexander Smola. A kernel two-sample test. *The journal of machine learning research*, 13(1):723–773, 2012.
49. Wei Zuo, Fei Huang, Y Jeffrey Chiang, Meng Li, Jun Du, Yi Ding, Ting Zhang, Hyuk Woo Lee, Lak Shin Jeong, Yuling Chen, et al. c-Cbl-mediated neddylation antagonizes ubiquitination and degradation of the TGF- β type II receptor. *Molecular cell*, 49(3):499–510, 2013.
50. Edward Y Chen, Christopher M Tan, Yan Kou, Qiaonan Duan, Zichen Wang, Gabriela Vaz Meirelles, Neil R Clark, and Avi Ma’ayan. Enrichr: interactive and collaborative HTML5 gene list enrichment analysis tool. *BMC bioinformatics*, 14(1):128, 2013.
51. Arthur Liberzon, Aravind Subramanian, Reid Pinchback, Helga Thorvaldsdóttir, Pablo Tamayo, and Jill P Mesirov. Molecular signatures database (MSigDB) 3.0. *Bioinformatics*, 27(12):1739–1740, 2011. Version: 2025.1.Hs.
52. Yoav Benjamini and Yosef Hochberg. Controlling the false discovery rate: a practical and powerful approach to multiple testing. *Journal of the Royal statistical society: series B (Methodological)*, 57(1):289–300, 1995.
53. Sergey Brin, Rajeev Motwani, Jeffrey D Ullman, and Shalom Tsur. Dynamic itemset counting and implication rules for market basket data. In *Proceedings of the 1997 ACM SIGMOD international conference on Management of data*, pages 255–264, 1997.
54. Jonas Peters, Peter Bühlmann, and Nicolai Meinshausen. Causal inference by using invariant prediction: identification and confidence intervals. *Journal of the Royal Statistical Society Series B: Statistical Methodology*, 78(5):947–1012, 2016.
55. Karren Yang, Abigail Katcoff, and Caroline Uhler. Characterizing and learning equivalence classes of causal DAGs under interventions. In *International Conference on Machine Learning*, pages 5541–5550. PMLR, 2018.
56. Jiaqi Zhang, Kristjan Greenewald, Chandler Squires, Akash Srivastava, Karthikeyan Shanmugam, and Caroline Uhler. Identifiability guarantees for causal disentanglement from soft interventions. *Advances in Neural Information Processing Systems*, 36:50254–50292, 2023.
57. Haofei Wang, Yuchen Yang, Jiandong Liu, and Li Qian. Direct cell reprogramming: approaches, mechanisms and progress. *Nature Reviews Molecular Cell Biology*, 22(6):410–424, 2021.
58. Reza Bayat Mokhtari, Tina S Homayouni, Narges Baluch, Evgeniya Morgatskaya, Sushil Kumar, Bikul Das, and Herman Yeger. Combination therapy in combating cancer. *Oncotarget*, 8(23):38022, 2017.
59. Sanjay R Srivatsan, José L McFalone-Figueroa, Vijay Ramani, Lauren Saunders, Junyue Cao, Jonathan Packer, Hannah A Pliner, Dana L Jackson, Riza M Daza, Lena Christiansen, et al. Massively multiplex chemical transcriptomics at single-cell resolution. *Science*, 367(6473):45–51, 2020.
60. David Van Dijk, Roshan Sharma, Juozas Nainys, Kristina Yim, Pooja Kathail, Ambrose J Carr, Cassandra Burdziak, Kevin R Moon, Christine L Chaffer, Diwakar Pattabiraman, et al. Recovering gene interactions from single-cell data using data diffusion. *Cell*, 174(3):716–729, 2018.
61. Herbert E Robbins. An empirical Bayes approach to statistics. In *Proceedings of the Third Berkeley Symposium on Mathematical Statistics and Probability (1954/1955), Vol. I*, pages 157–163. University of California Press, 1956.
62. Peter J Diggle and Richard J Gratton. Monte Carlo methods of inference for implicit statistical models. *Journal of the Royal Statistical Society Series B: Statistical Methodology*, 46(2):193–212, 1984.
63. Pascal Vincent. A connection between score matching and denoising autoencoders. *Neural computation*, 23(7):1661–1674, 2011.
64. Yang Song and Stefano Ermon. Generative modeling by estimating gradients of the data distribution. *Advances in neural information processing systems*, 32, 2019.
65. Simo Särkkä and Arno Solin. *Applied stochastic differential equations*, volume 10. Cambridge University Press, 2019.
66. Yang Song, Jascha Sohl-Dickstein, Diederik P Kingma, Abhishek Kumar, Stefano Ermon, and Ben Poole. Score-based generative modeling through stochastic differential equations. In *International Conference on Learning Representations*, 2021.
67. Vincent Dumoulin, Jonathon Shlens, and Manjunath Kudlur. A learned representation for artistic style. In *International Conference on Learning Representations*, 2017.
68. Ashish Vaswani, Noam Shazeer, Niki Parmar, Jakob Uszkoreit, Llion Jones, Aidan N Gomez, Łukasz Kaiser, and Illia Polosukhin. Attention is all you need. *Advances in neural information processing systems*, 30, 2017.
69. Diederik Kingma and Jimmy Ba. Adam: A method for stochastic optimization. In *International Conference on Learning Representations*, 2015.
70. Sadie Beckett, Joshua Jee, Thapelo Ncube, Sophia Pompilus, Quintel Washington, Anshuman Singh, and Nabendu Pal. Zero-inflated Poisson (ZIP) distribution: Parameter estimation and applications to model data from natural calamities. *Involve, a Journal of Mathematics*, 7(6):751–767, 2014.
71. Rahul Satija, Jeffrey A Farrell, David Gennert, Alexander F Schier, and Aviv Regev. Spatial reconstruction of single-cell gene expression data. *Nature biotechnology*, 33(5):495–502, 2015.
72. P. Erdős and A Rényi. On random graphs. *Publicationes Mathematicae*, 6:290–297, 1959.
73. Albert-László Barabási and Réka Albert. Emergence of scaling in random networks. *Science*, 286(5439):509–512, 1999.
74. David J Hand and Robert J Till. A simple generalisation of the area under the ROC curve for multiple class classification problems. *Machine learning*, 45:171–186, 2001.

75. R. Penrose. On best approximate solutions of linear matrix equations. *Mathematical Proceedings of the Cambridge Philosophical Society*, 52(1):17–19, 1956.
76. Gene H Golub and Charles F Van Loan. *Matrix computations*. The Johns Hopkins University Press, 4th edition, 2013.
77. Andrei N. Tikhonov and Vasilii Y. Arsenin. *Solutions of Ill-posed Problems*. Winston and Sons, 1977.
78. Pauli Virtanen, Ralf Gommers, Travis E. Oliphant, Matt Haberland, Tyler Reddy, David Cournapeau, Evgeni Burovski, Pearu Peterson, Warren Weckesser, Jonathan Bright, Stéfan J. van der Walt, Matthew Brett, Joshua Wilson, K. Jarrod Millman, Nikolay Mayorov, Andrew R. J. Nelson, Eric Jones, Robert Kern, Eric Larson, C J Carey, İlhan Polat, Yu Feng, Eric W. Moore, Jake VanderPlas, Denis Laxalde, Josef Perktold, Robert Cimrman, Ian Henriksen, E. A. Quintero, Charles R. Harris, Anne M. Archibald, Antônio H. Ribeiro, Fabian Pedregosa, Paul van Mulbregt, and SciPy 1.0 Contributors. SciPy 1.0: Fundamental Algorithms for Scientific Computing in Python. *Nature Methods*, 17:261–272, 2020.
79. Gábor J. Székely, Maria L. Rizzo, and Nail K. Bakirov. Measuring and testing dependence by correlation of distances. *The Annals of Statistics*, 35(6):2769–2794, 2007.
80. Werner Zellinger, Thomas Grubinger, Edwin Lughofer, Thomas Natschläger, and Susanne Saminger-Platz. Central moment discrepancy (CMD) for domain-invariant representation learning. In *International Conference on Learning Representations*, 2017.

Supplementary Information

CLIPR Under Change of Variables

When performing a variable transformation of the states \mathbf{x} before learning a drift f , learned drifts will operate in different unit scales than the original state distribution $p(\mathbf{x})$. Our goal is to obtain CLIPR estimates for f in original units given only access to the transformation parameters and the learned f . To accomplish this, the following theorem provides the original drift as an explicit function of the transformation and the learned drift, assuming the diffusion scale is fixed:

Theorem 3. *Let $f^s(\mathbf{s}) = -\nabla u(\mathbf{s})$ be the drift of an SDE $d\mathbf{s}(t) = f^s(\mathbf{s}(t))dt + \sigma d\mathbb{W}(t)$ with $u : \mathbb{R}^d \rightarrow \mathbb{R}$ that induces stationary distribution $p(\mathbf{s})$. Suppose the variables are transformed as $\mathbf{x} = \mathbf{m} + \mathbf{T}\mathbf{s}$, where $\mathbf{m} \in \mathbb{R}^d$ and $\mathbf{T} \in \mathbb{R}^{d \times d}$ is positive definite. Then, the drift $f^x(\mathbf{x})$ of an SDE that induces the stationary distribution $p(\mathbf{x})$ with the same diffusion scale σ is*

$$f^x(\mathbf{x}) = \mathbf{T}^{-1}f^s(\mathbf{T}^{-1}(\mathbf{x} - \mathbf{m})).$$

Theorem 3 derives the drift of an SDE with the same diffusion scale σ as the original SDE, because σ is typically not changed based on a priori transformations such as data standardization. Without fixing σ , the transformed drift follows directly from Itô's Lemma (32) and restrictions on f and the transform can be relaxed. The gradient field and integrability condition ensure that f induces a stationary distribution and has zero curl. Since we train the drift f with score matching, which approximately yields a gradient field, Theorem 3 can be used for analyzing LCD drifts despite the standardization used in training. The following corollary gives the perturbation responses of the drift f^x in Theorem 3 as an explicit function of f^s and the parameters of the transform:

Corollary 4. *The perturbation responses of f^x in Theorem 3 can be expressed in terms of f^s as*

$$\begin{aligned} \mathbf{v}_{f^x} &= \mathbf{T}^{-1}f^s(-\mathbf{T}^{-1}\mathbf{m}), \\ \mathbf{l}_{f^x} &= \mathbf{m} + \mathbf{T}\mathbf{l}_{f^s}. \end{aligned}$$

Proof of Theorem 1

We seek the parameter matrix \mathbf{A} that induces the perturbation response vectors $\{\mathbf{v}_{f_{q_1}}, \dots, \mathbf{v}_{f_{q_k}}\}$ and $\{\mathbf{l}_{f_{q_1}}, \dots, \mathbf{l}_{f_{q_k}}\}$ under the linear model (Eq. 3) with the least squared approximation error and minimum Frobenius norm.

By definition of \tilde{f}_q , it must hold that $\mathbf{v}_{f_q} = \mathbf{b} + \mathbf{c}_q$ for the linear model to induce the initial perturbation response \mathbf{v}_{f_q} . Moreover, since the post-perturbation mean $\boldsymbol{\mu}_q$ is the unique fixed point of the linear drift, the linear model must satisfy $\mathbf{l}_{f_q} = \boldsymbol{\mu}_q$. Substituting both conditions into the analytical form of the mean (Eq. 4), we obtain the equality $\mathbf{A}\mathbf{l}_{f_q} = -\mathbf{v}_{f_q}$. Combining the conditions for all perturbations $\{q_1, \dots, q_k\}$, we obtain the system of linear equations

$$\mathbf{AL} = -\mathbf{V}, \tag{17}$$

where \mathbf{V} and \mathbf{L} are defined as in the theorem statement. If \mathbf{A} satisfies the equality (Eq. 17), the linear SDE model with causal effects \mathbf{A} induces exactly the perturbation responses specified by \mathbf{V} and \mathbf{L} .

In general, this system may, however, be underdetermined (infinitely many solutions \mathbf{A}) or inconsistent (no solution \mathbf{A}). We therefore seek the least squares solution $\hat{\mathbf{A}} = \arg \min_{\mathbf{A}} \|\mathbf{AL} + \mathbf{V}\|_F^2$ with minimum norm $\|\mathbf{A}\|_F^2$, which always exists, is unique, and is given by the Moore-Penrose pseudoinverse (75)

$$\hat{\mathbf{A}} = -\mathbf{VL}^+.$$

Moreover, if $\mathbf{L} \in \mathbb{R}^{d \times k}$ has full row rank, $\hat{\mathbf{A}}$ is the only least squared solution (76). Thus, if additionally an exact solution \mathbf{A} of Eq. 17 exists, where the least squared error is minimized at zero, the matrix

$\widehat{\mathbf{A}}$ uniquely identifies this solution. This implies that $\widehat{\mathbf{A}} = \mathbf{A}$ if the perturbation response matrices \mathbf{V} and \mathbf{L} are generated by a linear drift $f = \tilde{f}$, where an exact solution exists (the true \mathbf{A}), and \mathbf{L} has full row rank. A sufficient condition for \mathbf{L} being full row rank is that $k \geq d$ perturbation shift vectors \mathbf{c}_{q_i} are linearly independent. This fails only in the degenerate case where \mathbf{b} is an affine combination of the perturbation shifts, i.e., $\mathbf{b} = \sum_{i=1}^k \beta_i \mathbf{c}_{q_i}$ with $\sum_{i=1}^k \beta_i = 1$. Otherwise, the vectors $\mathbf{b} + \mathbf{c}_{q_i} = \mathbf{l}_{f_{q_i}}$ are linearly independent, so \mathbf{L} has full rank.

When Eq. 17 is inconsistent, the least squares solution $\widehat{\mathbf{A}}$ may not be optimal in all applications. The estimator can be made more well-behaved by regularizing the norm of the solution itself via $\widehat{\mathbf{A}}_\lambda = \arg \min_{\mathbf{A}} \|\mathbf{AL} + \mathbf{V}\|_2^2 + \lambda \|\mathbf{A}\|_2^2$, known as Tikhonov regularization. The analytical solution to this regularized problem is given by (77)

$$\widehat{\mathbf{A}}_\lambda = -\mathbf{VL}^\top (\mathbf{LL}^\top + \lambda \mathbf{I})^{-1}.$$

■

Proof of Corollary 2

The linear system (Eq. 3) with CLIPR matrix $\widehat{\mathbf{A}}$ satisfies Eq. 4. By definition, $\mathbf{c}_q = 0$ for the unperturbed drift f , so $\boldsymbol{\mu} = \mathbf{l}_f = -\widehat{\mathbf{A}}^{-1}\mathbf{b}$ and thus $\mathbf{b} = -\widehat{\mathbf{A}}\mathbf{l}_f$. Following the same reasoning, the perturbation vectors \mathbf{c}_q are given by $\mathbf{c}_q = -\mathbf{b} - \widehat{\mathbf{A}}\mathbf{l}_{f_q}$.

■

Proof of Theorem 3

To prove the statement, we first establish the following fact:

Lemma 5. *Let $u : \mathbb{R}^d \rightarrow \mathbb{R}$ be a function such that $\exp(-2u(\mathbf{x}))$ is integrable. For any positive definite matrix $\boldsymbol{\Gamma}$, the SDE*

$$d\mathbf{x}(t) = -\boldsymbol{\Gamma} \nabla u(\mathbf{x}(t)) dt + \boldsymbol{\Gamma}^{1/2} d\mathbb{W}(t) \quad (18)$$

has stationary distribution

$$p(\mathbf{x}) \propto \exp(-2u(\mathbf{x})),$$

which is independent of the scaling matrix $\boldsymbol{\Gamma}$.

Proof The Fokker-Planck equation (65) for the SDE (Eq. 18) states that the time evolution of the density $p(\mathbf{x}, t)$ is given by

$$\frac{\partial}{\partial t} p(\mathbf{x}, t) = -\nabla \cdot J(\mathbf{x}, t),$$

where the probability flow is

$$J(\mathbf{x}, t) = -\boldsymbol{\Gamma} \nabla u(\mathbf{x}) p(\mathbf{x}, t) - \frac{1}{2} \boldsymbol{\Gamma} \nabla p(\mathbf{x}, t).$$

A distribution $p(\mathbf{x})$ is stationary if and only if $\frac{\partial}{\partial t} p(\mathbf{x}, t) = 0$, which by the Fokker-Planck equation is equivalent to $\nabla \cdot J(\mathbf{x}) = 0$ for all \mathbf{x} . A sufficient condition for this is that the probability current itself vanishes, i.e. $J(\mathbf{x}) = \mathbf{0}$. We verify that $p(\mathbf{x}) \propto \exp(-2u(\mathbf{x}))$ satisfies this condition. For this choice of $p(\mathbf{x})$, we have

$$\nabla p(\mathbf{x}) = -2p(\mathbf{x}) \nabla u(\mathbf{x}).$$

Substituting into the expression for $J(\mathbf{x})$ yields

$$J(\mathbf{x}) = -\boldsymbol{\Gamma} \nabla u(\mathbf{x}) p(\mathbf{x}) - \frac{1}{2} \boldsymbol{\Gamma} \nabla p(\mathbf{x}) = -\boldsymbol{\Gamma} \nabla u(\mathbf{x}) p(\mathbf{x}) + \boldsymbol{\Gamma} \nabla u(\mathbf{x}) p(\mathbf{x}) = \mathbf{0}.$$

Thus, $p(\mathbf{x}) \propto \exp(-2u(\mathbf{x}))$ is a stationary distribution, and this form is independent of $\mathbf{\Gamma}$. The integrability condition ensures that the normalization constant is finite, so that $p(\mathbf{x})$ is a valid probability density. ■

We now prove the main result. Given a transformation $\mathbf{x} = \phi(\mathbf{s})$, the stochastic processes $\mathbf{x}(t)$ is obtained from $\mathbf{s}(t)$ by

$$\mathbf{x}(t) = \phi(\mathbf{s}(t)) = \mathbf{m} + \mathbf{T}\mathbf{s}(t).$$

By Itô's Lemma (32) applied to the general SDE form and ϕ , the SDE for $\mathbf{x}(t)$ is

$$\begin{aligned} d\mathbf{x}(t) &= \nabla\phi(\mathbf{s}(t)) d\mathbf{s}(t) \\ &= \mathbf{T}(f(\mathbf{s}(t))dt + \sigma d\mathbb{W}t) \\ &= \mathbf{T}f(\mathbf{s}(t))dt + \sigma\mathbf{T}d\mathbb{W}t \\ &= \mathbf{T}f(\mathbf{T}^{-1}(\mathbf{x}(t) - \mathbf{m}))dt + \sigma\mathbf{T}d\mathbb{W}t \end{aligned} \tag{19}$$

This SDE induces the transformed stationary distribution $p(\mathbf{x})$. However, the diffusion scale in Eq. 19 is $\sigma\mathbf{T}$, while we seek the SDE with the same diffusion scale σ as the original SDE. Lemma 5 shows that a constant positive definite scaling $\mathbf{\Gamma}$ does not change the stationary distribution. Hence, we apply the scaling factor $\mathbf{\Gamma} = \mathbf{T}^{-2}$ to Eq. 19. This yields

$$d\tilde{\mathbf{x}}(t) = \mathbf{T}^{-1}f(\mathbf{T}^{-1}(\tilde{\mathbf{x}}(t) - \mathbf{m}))dt + \sigma d\mathbb{W}t,$$

which induces the correct transformed stationary distribution with the original diffusion scale σ . ■

Proof of Corollary 4

By Theorem 3, the drift f^x is given by $f^x(\mathbf{x}) = \mathbf{T}^{-1}f^s(\mathbf{T}^{-1}(\mathbf{x} - \mathbf{m}))$. Since $\mathbf{v}_{f^x} = f^x(\mathbf{0})$ by definition, we have

$$\mathbf{v}_{f^x} = \mathbf{T}^{-1}f^s(-\mathbf{T}^{-1}\mathbf{m}).$$

Moreover, the fixed point \mathbf{x}^* of f^x satisfies

$$f^x(\mathbf{x}^*) = \mathbf{0} \Leftrightarrow f^s(\mathbf{T}^{-1}(\mathbf{x}^* - \mathbf{m})) = \mathbf{0}$$

Since the fixed point \mathbf{s}^* of f^s satisfies $f^s(\mathbf{s}^*) = \mathbf{0}$, we have $\mathbf{s}^* = \mathbf{T}^{-1}(\mathbf{x}^* - \mathbf{m})$, and conversely, $\mathbf{x}^* = \mathbf{m} + \mathbf{T}\mathbf{s}^*$. Thus,

$$\mathbf{l}_{f^x} = \mathbf{m} + \mathbf{T}\mathbf{l}_{f^s}.$$
■

Example: Linear SDEs and Gaussian distributions

In this section, we illustrate Theorem 1 and Corollary 2 by applying them to linear SDEs (Eq. 3), for which the stationary distribution is known analytically. Consider an SDE system with drift $f^s(\mathbf{s})$ that induces a Gaussian stationary distribution $\mathbf{s} \sim \mathcal{N}(\boldsymbol{\mu}, \mathbf{P}^{-1})$. We apply the elementwise transformation

$$\mathbf{x} = \phi(\mathbf{s}) = \mathbf{m} + \mathbf{T}\mathbf{s},$$

where \mathbf{T} is positive definite. Under this transformation, \mathbf{x} remains Gaussian with $\mathbf{x} \sim \mathcal{N}(\mathbf{m} + \mathbf{T}\boldsymbol{\mu}, \mathbf{T}\mathbf{P}^{-1}\mathbf{T}^T)$. Our goal is to derive the drift and causal effects of an SDE inducing the stationary distribution $p(\mathbf{x})$ using only the drift $f^s(\mathbf{s})$ of an SDE inducing the stationary distribution $p(\mathbf{s})$ and the transformation ϕ , keeping the diffusion scale fixed.

We begin with a drift f^s inducing the stationary distribution $p(\mathbf{s})$. For a Gaussian distribution, we have $\nabla \log p(\mathbf{s}) = -\mathbf{P}(\mathbf{s} - \boldsymbol{\mu})$. An SDE with stationary distribution $p(\mathbf{s})$ is thus the Langevin diffusion with

$$d\mathbf{s}(t) = -\mathbf{P}(\mathbf{s}(t) - \boldsymbol{\mu})dt + \sqrt{2}d\mathbb{W}(t).$$

This identifies the drift $f^s(\mathbf{s})$ and the causal matrix \mathbf{A}_s of the linear model (Eq. 3) as

$$f^s(\mathbf{s}) = -\mathbf{P}(\mathbf{s} - \boldsymbol{\mu}) \quad \mathbf{A}_s = -\mathbf{P}.$$

We now apply our results to obtain the parameters of an SDE inducing $p(\mathbf{x})$.

Theorem 3: Since $f^s(\mathbf{s})$ is the gradient of a potential and the SDE admits a stationary distribution, Theorem 3 can be directly applied to obtain the drift $f^x(\mathbf{x})$ of an SDE inducing $p(\mathbf{x})$ as its stationary distribution with the same diffusion scale:

$$f^x(\mathbf{x}) = \mathbf{T}^{-1}f^s(\mathbf{T}^{-1}(\mathbf{x} - \mathbf{m})) = -\mathbf{T}^{-1}\mathbf{P}\mathbf{T}^{-1}(\mathbf{x} - \mathbf{m} - \mathbf{T}\boldsymbol{\mu}).$$

As expected, this matches the drift derived directly from the closed form of $p(\mathbf{x})$ by computing $\nabla \log p(\mathbf{x})$. The corresponding matrix \mathbf{A}_x of f^x in Eq. 3 is

$$\mathbf{A}_x = -\mathbf{T}^{-1}\mathbf{P}\mathbf{T}^{-1}.$$

Corollary 4: Applying Corollary 4, the perturbation responses of f^x are

$$\begin{aligned} \mathbf{v}_{f^x} &= \mathbf{T}^{-1}f^s(-\mathbf{T}^{-1}\mathbf{m}) = \mathbf{T}^{-1}\mathbf{P}\mathbf{T}^{-1}(\mathbf{m} + \mathbf{T}\boldsymbol{\mu}) \\ \mathbf{l}_{f^x} &= \mathbf{m} + \mathbf{T}\mathbf{l}_{f^s} = \mathbf{m} + \mathbf{T}\boldsymbol{\mu} \end{aligned}$$

As shown in Theorem 1, the causal matrix \mathbf{A}_x of f^x must satisfy

$$\mathbf{A}_x \mathbf{l}_{f^x} = -\mathbf{v}_{f^x}.$$

Substituting the expressions for \mathbf{v}_{f^x} and \mathbf{l}_{f^x} , we obtain the condition

$$\mathbf{A}_x(\mathbf{m} + \mathbf{T}\boldsymbol{\mu}) = -\mathbf{T}^{-1}\mathbf{P}\mathbf{T}^{-1}(\mathbf{m} + \mathbf{T}\boldsymbol{\mu}),$$

confirming that the matrix \mathbf{A}_x derived from $f^x(\mathbf{x})$ exactly satisfies the constraints specified by \mathbf{v}_{f^x} and \mathbf{l}_{f^x} in Corollary 4.

Gene Interaction Classification

We follow the framework by Norman et al. (4) to classify gene pairs into gene interaction (GI) types. Their approach measures GIs by comparing the mean expression of double gene perturbations to those of the constituent single gene perturbations. Since the data by Wessels et al. (5) does not contain sufficient single gene perturbations to cover a substantial number of double perturbations, our GI analysis focuses on the data by Norman et al. (4) (Table S1).

Our experiments were performed on a selection of $d = 1000$ highly variable genes (Methods). Following Norman et al., we performed GI type classifications based on the $p = 570$ genes with a minimum mean unique molecular identifier (UMI) count of 0.5. We define:

- $\boldsymbol{\delta}_a \in \mathbb{R}^p$: differential expression vector for perturbation q_a
- $\boldsymbol{\delta}_b \in \mathbb{R}^p$: differential expression vector for perturbation q_b
- $\boldsymbol{\delta}_{a,b} \in \mathbb{R}^p$: differential expression vector for the combinatorial perturbation of q_a and q_b

Here, differential expression denotes the difference in mean counts between the perturbation and control (q_0) data after library standardization. Let $c_a, c_b \in \mathbb{R}$ be the regression coefficients obtained by fitting

$$[\boldsymbol{\delta}_{a,b}]_g = c_a[\boldsymbol{\delta}_a]_g + c_b[\boldsymbol{\delta}_b]_g + \epsilon_g,$$

for each gene $g \in \{1, \dots, p\}$, where ϵ_g denotes the residual error. The parameters are estimated using robust (Theil-Sen) regression to reduce sensitivity to outliers and skewness. We use the implementation by SciPy (78) with 10^5 randomly selected data point pairs and 10^3 iterations for computing the spatial median of the two coefficients.

Norman et al. define four metrics for characterizing GIs (Table S2). These metrics quantify: (i) the magnitude of c_a and c_b ; (ii) the similarity among $\boldsymbol{\delta}_a$, $\boldsymbol{\delta}_b$, and $\boldsymbol{\delta}_{a,b}$, measured via distance correlation (79); (iii) the quality of the linear fit for $\boldsymbol{\delta}_{a,b}$; and (iv) the equality of contribution of $\boldsymbol{\delta}_a$ and $\boldsymbol{\delta}_b$ in explaining $\boldsymbol{\delta}_{a,b}$. Based on these metrics, Norman et al. classify GIs into six categories: suppression, additivity, synergy, epistasis, redundancy, and neomorphism.

The original GI classifications by Norman et al. (4) were annotated based on GI metrics computed over the full gene set, whereas our analysis focused on $d = 1000$ highly variable genes. Although our metrics remain strongly correlated to those computed in the original study, preprocessing choices and gene selection affect their values and thus the GI classifications (Fig. S3). We therefore re-calibrated the classification thresholds for our gene set, following an approach similar to that of Roohani et al. (17). Specifically, we determined the GI metric thresholds required to recover the original GI annotations given the metrics computed under our gene selection (for robustness considering 5–95 percentiles of the computed metrics) (Fig. S4). The resulting thresholds are provided in Table S3 and were used to classify all available double gene perturbations.

Maximum Mean Discrepancy

We benchmarked methods by comparing a predicted set of N samples $\widehat{\mathbf{Y}}_q$ for perturbation q to the N_q observed post-perturbation samples \mathbf{Y}_q , following library size standardization and log transformation (Methods). Our primary metric was the maximum mean discrepancy (MMD), which quantifies the discrepancy between two distributions (48). Specifically, we computed an unbiased empirical estimate of the MMD with kernel k (48):

$$\begin{aligned} \text{MMD}(\widehat{\mathbf{Y}}_q, \mathbf{Y}_q) = & \frac{1}{N(N-1)} \sum_{n=1}^N \sum_{m \neq n}^N k(\widehat{\mathbf{y}}^{(n)}, \widehat{\mathbf{y}}^{(m)}) + \frac{1}{N_q(N_q-1)} \sum_{n=1}^{N_q} \sum_{m \neq n}^{N_q} k(\mathbf{y}^{(n)}, \mathbf{y}^{(m)}) \\ & - \frac{2}{NN_q} \sum_{n=1}^N \sum_{m=1}^{N_q} k(\widehat{\mathbf{y}}^{(n)}, \mathbf{y}^{(m)}). \end{aligned} \quad (20)$$

Baselines

We evaluated LCDs against various baseline methods. For GEARS (17)* and CPA (19)†, we used the original implementations by the authors. For SALT and PEPER (13), we used our own implementations. All baselines generated samples from the post-perturbation distribution by predicting a (mean) post-perturbation shift and then shifting samples from the control (q_0) data by the predicted offset. SALT, PEPER, and GEARS are designed to predict means only, and for CPA, this was the recommended approach in the implementation. As described in Methods, SALT predicts the post-perturbation shift of a double perturbation q_a, q_b as the sum $\Delta_{q_a} + \Delta_{q_b}$ of its constituent single post-perturbation shifts $\Delta_{q_a}, \Delta_{q_b} \in \mathbb{R}^d$. (13).

PEPER extends SALT by training a neural network correction that is added to the SALT offset $\Delta_{q_a} + \Delta_{q_b}$. Specifically, the method learns two multiplayer perceptrons (MLPs) ϕ_1 and ϕ_2 that predict the correction

*GEARS code repository: <https://github.com/snap-stanford/GEARS>

†CPA code repository: <https://github.com/theislab/cpa>

term as $\phi_2(\phi_1(\Delta_{q_a}) + \phi_1(\Delta_{q_b}))$ using the central moment discrepancy loss (80). The model was trained for 30,000 steps with batch size 256 using the Adam optimizer (69) with learning rate 0.001 and weight decay tuned over $\{0.1, 0.003, 0.0001\}$. We also tuned the number of MLP hidden layers over $\{1, 2\}$ and hidden sizes over $\{256, 1024\}$.

CPA trains an autoencoder using a Gaussian reconstruction loss and an adversarial cross entropy loss that encourages a separation of latent state and perturbation information. We tuned the latent state dimensionality over $\{64, 256\}$; encoder, decoder, and adversarial classifier hidden size over $\{1024, 2048, 4096\}$, weight decay over $\{10^{-5}, 10^{-8}\}$; dropout probability of all networks over $\{0.0, 0.2\}$; and the strength of the adversarial loss over $\{0.01, 1.0\}$. Training performed a maximum number of 1000 epochs, and all networks used 2 hidden layers. The method has additional hyperparameters, for which we selected defaults based on recommendations in the original implementation by the authors.

GEARS trains a graph neural network (GNN) over gene and perturbation relationship graphs constructed from prior knowledge databases. We optimized the GEARS model for 20 epochs and tuned the batch size over $\{32, 256\}$, the Pearson correlation threshold when constructing the co-expression graph over $\{0.4, 0.8\}$, the maximum similar genes considered in the graphs over $\{5, 10, 20\}$, and the number of GNN layers over $\{1, 2\}$. The remaining hyperparameters were kept at defaults suggested by the original implementation. Hyperparameter tuning is described in [Methods](#).

Computational Resources

We trained LCDs on an internal cluster with 1 GPU (20GiB) and 4 CPUs (24GiB each for Wessels. et al. and Norman et al. datasets; 120GiB each for Replogle et al. dataset). Inferring the implicit prior densities was more computationally intensive (~ 9 h; inference step 1) than training the drift (~ 1 h; inference step 2), because of the large number of Monte Carlo samples M needed to sufficiently reduce the bias of \mathcal{L}_{IP} and achieve good fit of the priors.

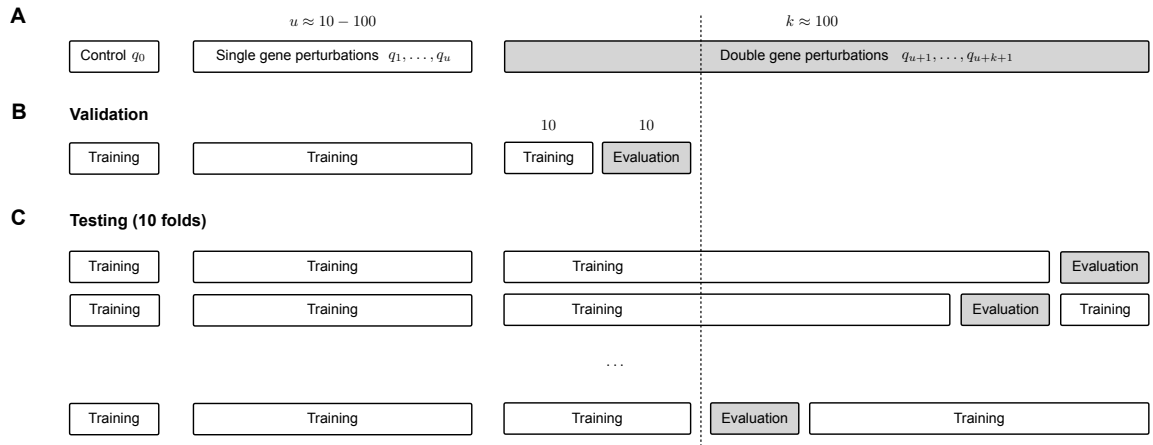


Figure S1: Training and evaluation splits of the combinatorial gene perturbation data by Wessels et al. (5) and Norman et al. (4) used for benchmarking (Fig. 2). (A) Each dataset contains control samples (q_0), u single gene perturbations, and k double gene perturbations. Control and single gene perturbation samples are always in the training set. **(B)** We reserved 20 double gene perturbations for hyperparameter tuning of each method (Methods), where 10 were included in the training set and 10 were used for evaluation. **(C)** For benchmarking, we evaluated methods on 10 disjoint testing folds of the held-out double perturbations. All perturbations used for hyperparameter tuning were included in the training set to avoid information leakage. Combining all testing folds, methods generated held-out predictions for all $k - 20$ held-out double perturbations.

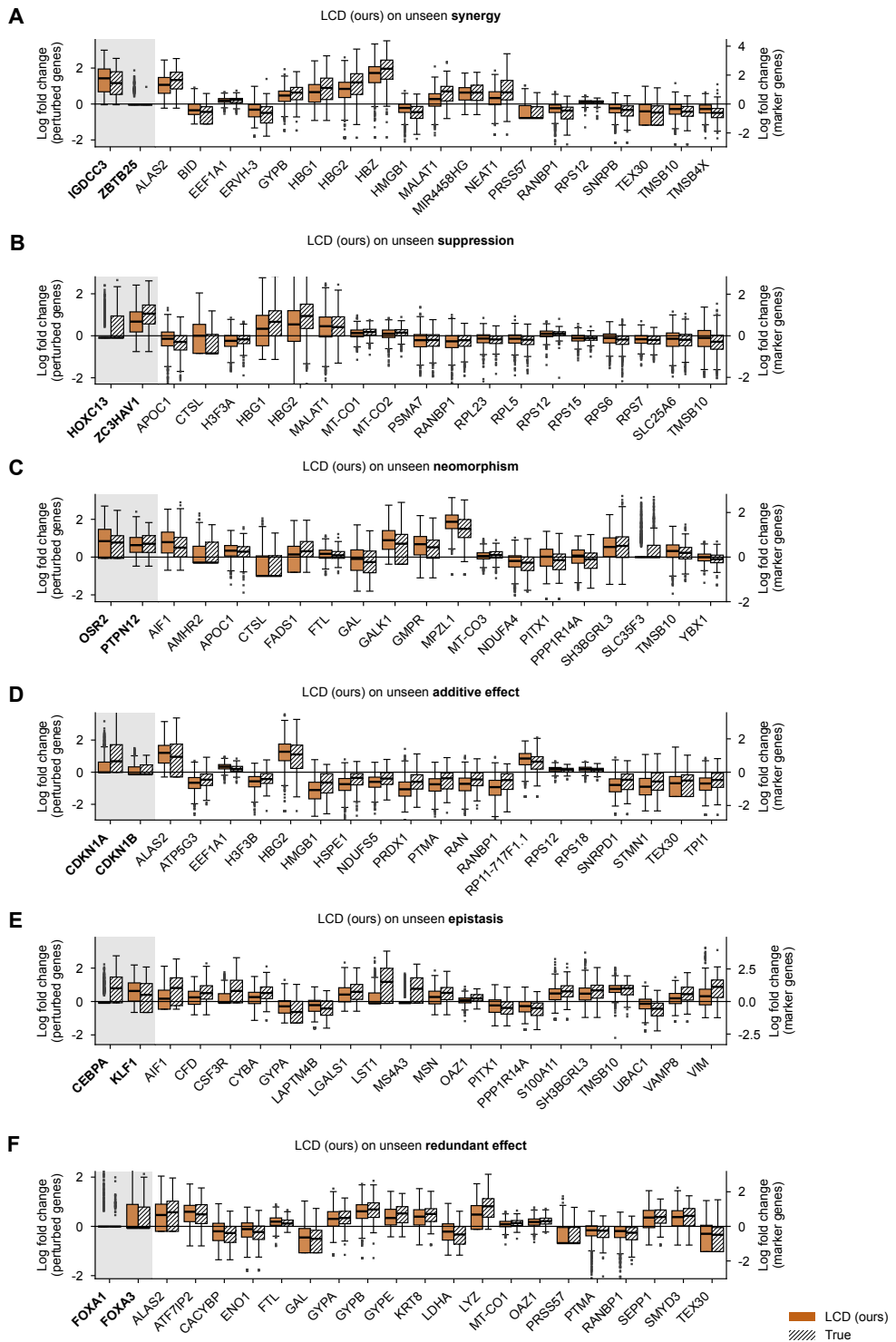


Figure S2: LCD predictions on two-gene perturbation combinations with different genetic interaction (GI) types. Predicted vs. observed expression for top 20 DE genes of a held-out perturbation with neomorphic GI. Grey section shows the perturbed genes (bold labels). All box plots show median and interquartile range.

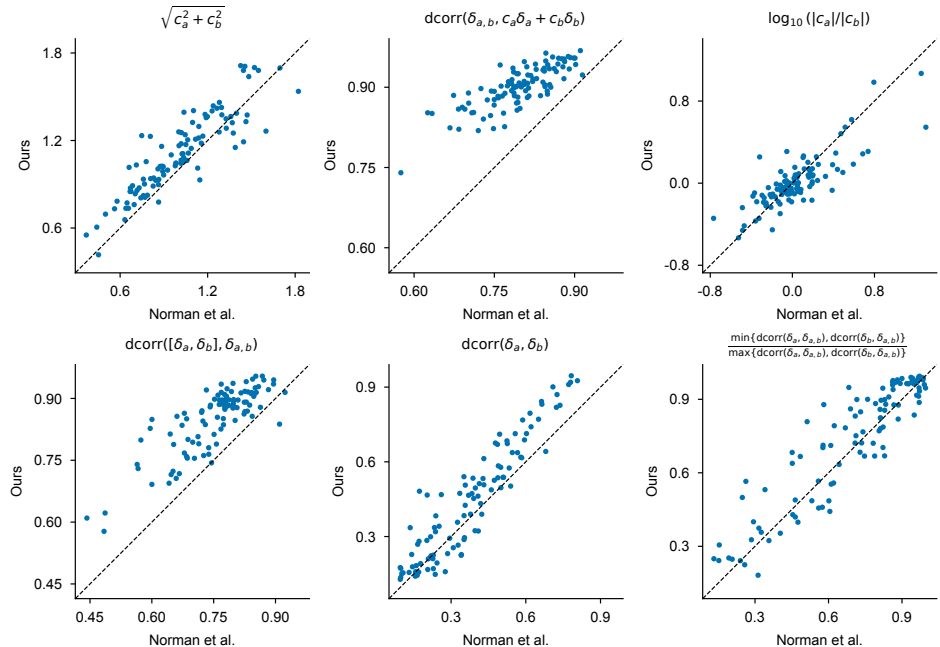


Figure S3: Comparison of gene interaction (GI) metrics between the original study (4) and our experiments. We selected $d = 1000$ highly variable genes and applied specific preprocessing steps for quality control, which affect the computed GI metrics. Our results show strong correlation with those from the original study, motivating our decision to calibrate GI type thresholds based on the original annotations (SI Appendix, Fig. S4). Each point represents a gene pair for which a double perturbation and both constituent single perturbations are available, thus enabling GI metric computation.

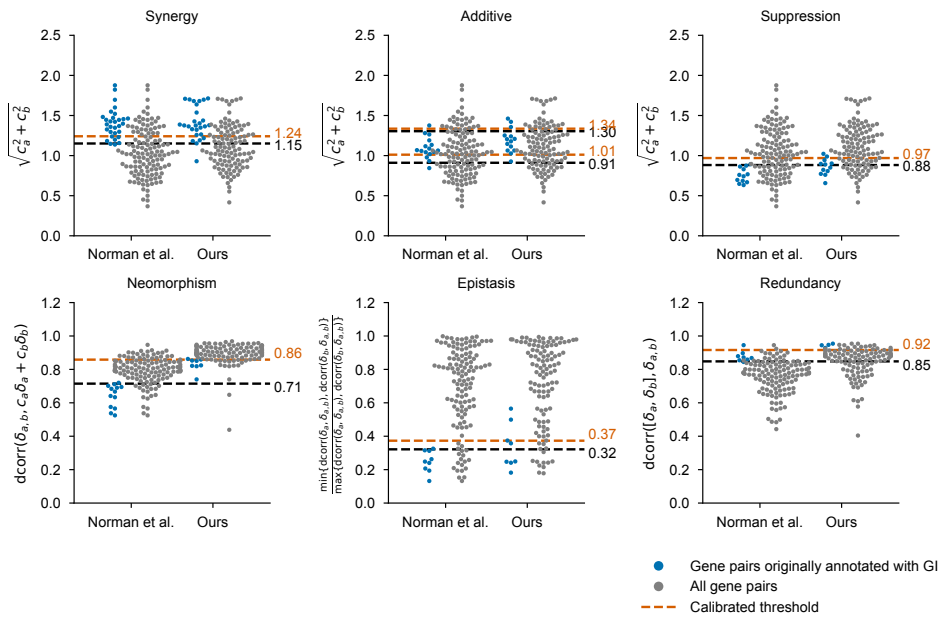


Figure S4: Calibration of gene interaction (GI) classification thresholds between the original study (4) and our experiments. Each panel corresponds to one of six GI categories, comparing the distribution of GI metrics from the original study (left) with those from our experiments (right). Blue points indicate gene pairs annotated with the respective GI type in the original study; grey points represent all available gene pairs. Black horizontal lines denote classification thresholds derived from the original annotations; red lines show thresholds calibrated to our metrics based on the scores of the originally annotated pairs. Thresholds are summarized in [SI Appendix, Table S3](#).

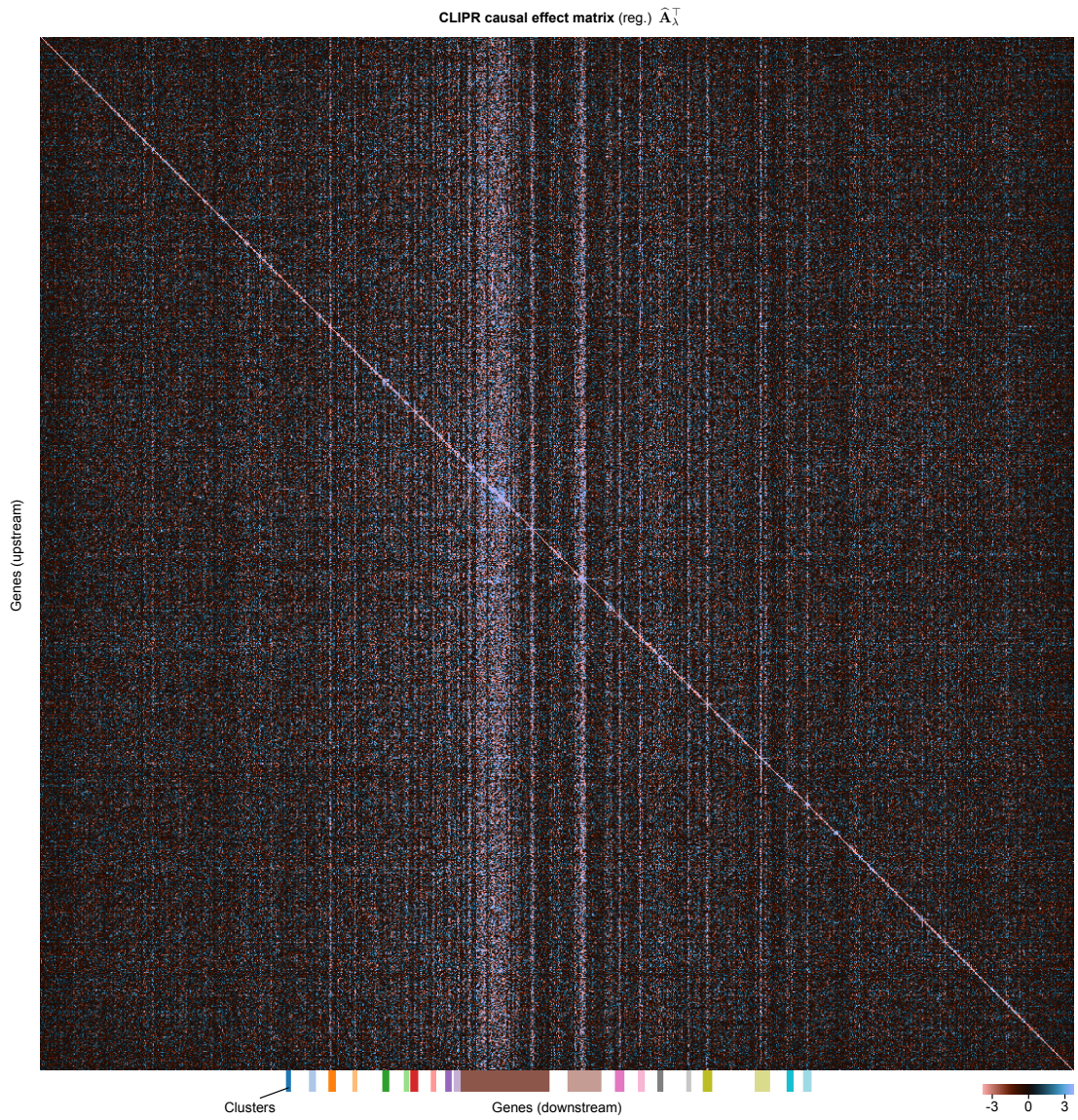


Figure S5: LCD-CLIPR estimate of the direct gene-gene causal effects among all $d = 1000$ modeled genes from the Perturb-seq screen by Replogle et al. (1). This plot complements Fig. 4B, where only genes assigned to clusters are shown for visual clarity. Clusters indicate those analyzed in the enrichment analysis. The matrix is transposed into graph adjacency orientation, so that entry (a, b) corresponds to the direct causal effect of gene a on gene b . Tikhonov regularization: $\lambda = 0.01$ (see Methods).

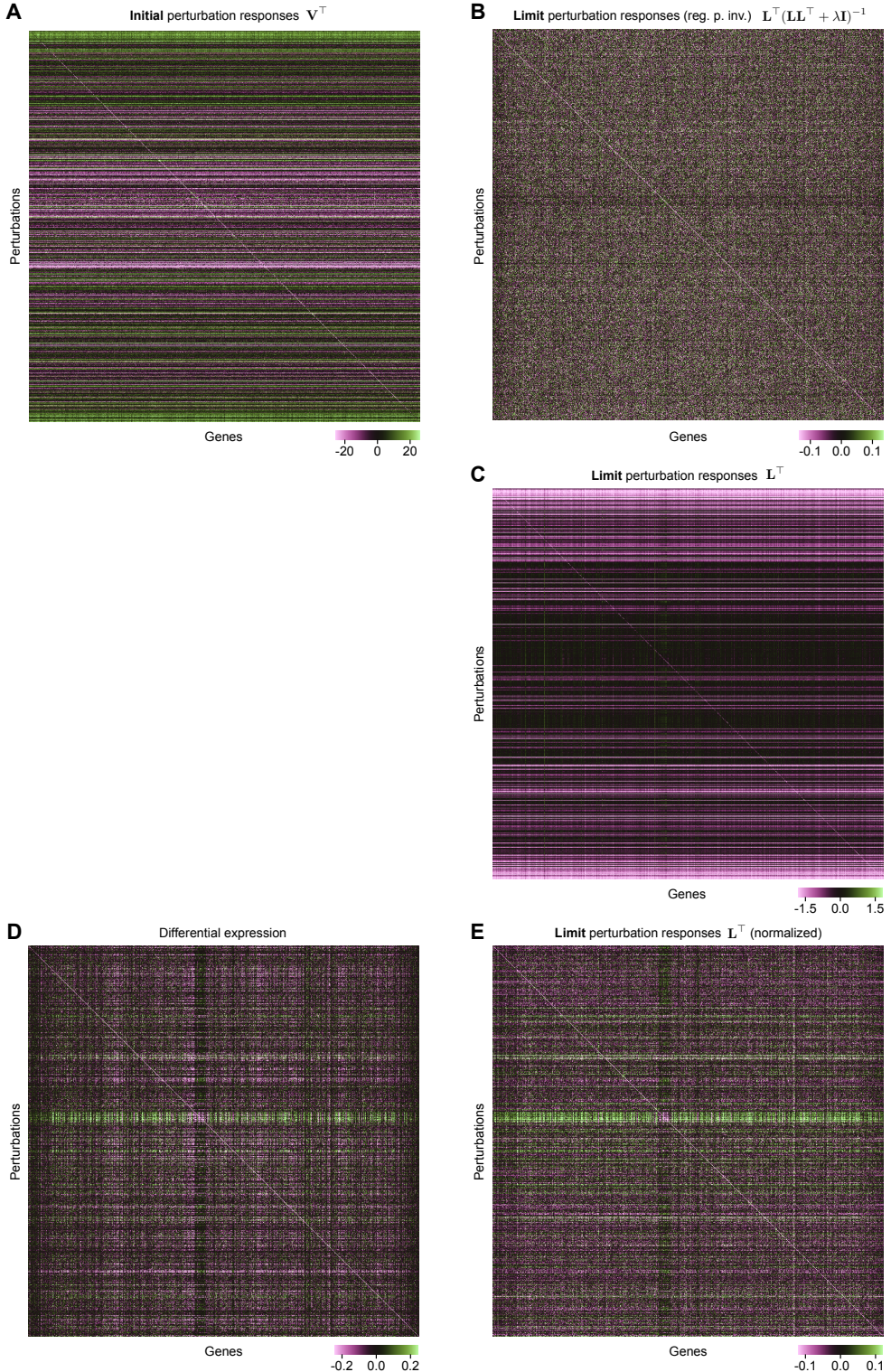


Figure S6: CLIPR components of the causal effects \hat{A}_λ in Fig. S5. This plot complements Fig. 4C, where only genes assigned to clusters are shown. (A) Initial perturbation responses (Eq. 5). (B) Tikhonov-regularized pseudoinverse of the limit perturbation responses. The CLIPR matrix \hat{A}_λ is equal to the (negative) product of (A, transposed) and (B). (C) Limit perturbation responses (Eq. 6). (D) Differential expressions observed in the data. (E) Limit perturbation responses, normalized by passing values through the Poisson rate functions μ_g , then applying the same library size standardization and log transformation used to preprocess the data. (E) corresponds closely to (D). Matrices are transposed with perturbation indices on the first axis. Perturbation on row g targets the gene on column g . Tikhonov regularization: $\lambda = 0.01$ (see Methods).

Table S1: Perturbation statistics of all datasets after preprocessing and gene selection.

Dataset	Perturbation	Cell line	Cells	Genes	Median cells per perturb.	One-gene perturbs.	Two-gene perturbs.	Genes perturbed
Wessels et al. (5)	Loss-of-function (knockdown; CaRPoool-seq)	THP-1	23,722	1000	175	5	104	25
Norman et al. (4)	Gain-of-function (overexpression; CRISPRa)	K562	96,804	1000	338	98	110	98
Replogle et al. (1)	Loss-of-function (knockdown; CRISPRi)	K562	209,462	1000	165	1000	–	1000

Table S2: Genetic interaction metrics following Norman et al. (4).

GI metric	Symbol	Definition
Magnitude	GI_{mag}	$\sqrt{c_a^2 + c_b^2}$
Similarity	GI_{sim}	$\text{dcorr}([\boldsymbol{\delta}_a, \boldsymbol{\delta}_b], \boldsymbol{\delta}_{a,b})$
Linear fit	GI_{fit}	$\text{dcorr}(\boldsymbol{\delta}_{a,b}, c_a \boldsymbol{\delta}_a + c_b \boldsymbol{\delta}_b)$
Equality of contribution	GI_{eq}	$\frac{\min\{\text{dcorr}(\boldsymbol{\delta}_a, \boldsymbol{\delta}_{a,b}), \text{dcorr}(\boldsymbol{\delta}_b, \boldsymbol{\delta}_{a,b})\}}{\max\{\text{dcorr}(\boldsymbol{\delta}_a, \boldsymbol{\delta}_{a,b}), \text{dcorr}(\boldsymbol{\delta}_b, \boldsymbol{\delta}_{a,b})\}}$

Table S3: Categories of genetic interactions based on the metrics in Table S2 following Norman et al. (4).

Category	Criterion	Description
Suppression	$GI_{mag} < 0.97$	Magnitude of double is smaller than expected from individual singles
Additivity	$0.97 < GI_{mag} < 1.34$	Magnitude of double is approximately equal to combination of singles
Synergy	$1.34 < GI_{mag}$	Magnitude of double is larger than expected from individual singles
Epistasis	$GI_{eq} < 0.37$	One perturbation dominates the other in explaining the double profile
Redundancy	$0.92 < GI_{sim}$	Single profiles strongly explain the profile of the double
Neomorphism	$GI_{fit} < 0.86$	Linear model does not provide good fit of the double profile